

# Geochemistry, Geophysics, Geosystems®



## RESEARCH ARTICLE

10.1029/2023GC010873

### Key Points:

- Cyclic fracturing, veining, and pressure solution are characteristic in the sediment-rich inner part (>250°C) of the accretionary wedge
- Synchrotron XFM documents pervasive micron-veinlets enabling layer-perpendicular fluid migration during slow wedge deformation
- Layer-parallel veins arrange in vein-arrays indicating localized fluid transport and potentially small seismic or slow-slip events

### Supporting Information:

Supporting Information may be found in the online version of this article.

### Correspondence to:

I. V. Akker,  
[vakker@erdw.ethz.ch](mailto:vakker@erdw.ethz.ch)

### Citation:

Akker, I. V., Schrank, C., Herwegh, M., Berger, A., Jones, M., & Kewish, C. M. (2023). The geometry, spatial distribution and texture of slate-hosted calcite veins in the Helvetic Flysch Units—Insights in structural and fluid processes within a paleo-accretionary complex. *Geochemistry, Geophysics, Geosystems*, 24, e2023GC010873. <https://doi.org/10.1029/2023GC010873>

Received 18 JAN 2023

Accepted 29 SEP 2023

### Author Contributions:

**Conceptualization:** Ismay Vénice Akker, Christoph Schrank, Marco Herwegh, Alfons Berger






**Data curation:** Ismay Vénice Akker, Christoph Schrank

**Formal analysis:** Ismay Vénice Akker, Christoph Schrank

**Funding acquisition:** Marco Herwegh

© 2023 The Authors. *Geochemistry, Geophysics, Geosystems* published by Wiley Periodicals LLC on behalf of American Geophysical Union. This is an open access article under the terms of the [Creative Commons Attribution License](https://creativecommons.org/licenses/by/4.0/), which permits use, distribution and reproduction in any medium, provided the original work is properly cited.

## The Geometry, Spatial Distribution and Texture of Slate-Hosted Calcite Veins in the Helvetic Flysch Units—Insights in Structural and Fluid Processes Within a Paleo-Accretionary Complex

Ismay Vénice Akker<sup>1,2</sup> , Christoph Schrank<sup>3,4,5</sup>, Marco Herwegh<sup>1</sup> , Alfons Berger<sup>1</sup> , Michael Jones<sup>4,6,7</sup> , and Cameron M. Kewish<sup>8,9</sup> 

<sup>1</sup>Institute of Geological Sciences, University of Bern, Bern, Switzerland, <sup>2</sup>Now at Structural Geology and Tectonics Group, Geological Institute, ETH Zürich, Zürich, Switzerland, <sup>3</sup>School of Earth and Atmospheric Science, Queensland University of Technology, Brisbane, QLD, Australia, <sup>4</sup>Planetary Surface Exploration, Queensland University of Technology, Brisbane, QLD, Australia, <sup>5</sup>Centre for Data Science, Queensland University of Technology, Brisbane, QLD, Australia, <sup>6</sup>Central Analytical Research Facility, Institute of Future Environments, Queensland University of Technology, Brisbane, QLD, Australia, <sup>7</sup>School of Chemistry and Physics, Queensland University of Technology, Brisbane, QLD, Australia, <sup>8</sup>Australian Nuclear Science and Technology Organisation, Australian Synchrotron, Clayton, VIC, Australia, <sup>9</sup>Department of Mathematical and Physical Sciences, School of Computing, Engineering and Mathematical Sciences, La Trobe University, Bundoora, VIC, Australia

**Abstract** The exhumed Infracentral Helvetic Flysch Units in the eastern central Alps in Switzerland are a field analog to modern accretionary wedges at active plate boundaries. In these seismically active convergent settings, water-saturated sediments undergo consolidation, and diagenetic to low-grade metamorphic processes cause complex fluid-rock interactions. To contribute to the understanding of structural and fluid processes and their interaction with seismic activity, we present quantitative information on the geometrical and spatial distribution of slate-hosted calcite veins from the Infracentral Helvetic Flysch Units that show mutual overprinting relationships with the ductile phyllosilicate-rich matrix. Two vein systems that form in the deeper part of the inner wedge are characterized: (a) layer-parallel veins (meter-scale) forming spatially repetitive vein-arrays and (b) pervasively distributed, steep micron-veinlets, that cross-cut the thicker layer-parallel veins and the ductile matrix. Synchrotron X-ray Fluorescence Microscopy (XFM) is instrumental in detecting previously unseen densely spaced micron-veinlets. The spatial distribution of micron-veinlets indicates pervasive layer-perpendicular fluid transport in response to dissolution-precipitation creep through the wedge. Layer-parallel veins form vein-arrays with thicknesses on the meter-scale suggesting that fluids are progressively localized in channels up-scale. Both vein sets form in an alternating fashion with two different enhanced flux directions, which could be indicative for a critically stressed wedge with near-lithostatic fluid pressures. The layer-parallel veins and vein-arrays could represent seismic events with low magnitude earthquakes (M<sub>w</sub> up to 4.0) or slow-slip events currently found at active plate boundaries, while micron-veinlets and dissolution-precipitation processes accommodate slow interseismic deformation.

**Plain Language Summary** Convergent plate boundaries are locations where lithospheric plates collide. Plate collision produces a wide variety of seismic activity, which is a major natural hazard posing socio-economic risks. When oceanic plates are involved in collision, an accretionary wedge made of sediments forms near the plate boundary. Here, we study an ancient accretionary wedge in the Swiss Alps to examine the potential traces of paleo-seismic activity left in the rock record. We focus on ubiquitous veins, mineralized fractures that acted as fluid pathways in such active seismic domains. We documented veins from the field (m-scale) to the grain scale (μm-scale). Synchrotron X-ray Fluorescence Microscopy (XFM) enabled mapping of trace-element concentrations in the vein minerals, capturing tracers of paleo-fluid transport at 2 μm resolution. The innovative XFM technique unveiled the presence of micron-veinlets with widths less than that of a human hair. These micron-veinlets form widespread, densely spaced clusters throughout these rock sequences. Our microanalytical observations demonstrate that these micron-veinlets facilitate fluid transport via dissolution-precipitation creep during interseismic deformation of the wedge while the m-scale veins could potentially represent small earthquakes or slow slip events.

**Investigation:** Ismay Vénice Akker, Christoph Schrank, Michael Jones, Cameron M. Kewish  
**Methodology:** Michael Jones, Cameron M. Kewish  
**Resources:** Marco Herwegh  
**Supervision:** Marco Herwegh, Alfons Berger  
**Validation:** Ismay Vénice Akker, Christoph Schrank, Alfons Berger  
**Visualization:** Ismay Vénice Akker, Christoph Schrank, Marco Herwegh  
**Writing – original draft:** Ismay Vénice Akker, Christoph Schrank, Marco Herwegh  
**Writing – review & editing:** Alfons Berger, Michael Jones, Cameron M. Kewish

## 1. Introduction

At convergent plate boundaries, sediments are accreted onto or subducted below a continental plate. This results in fault-bounded sediment packages forming an accretionary wedge (Dahlen, 1990; Davis et al., 1983). Along the plate boundary thrust, different types and styles of seismic activity are reported (e.g., Scholz, 1998; Schwartz & Rokosky, 2007) and deformational styles are affected by the rheological behavior of the subduction thrust (Dahlen, 1984; Davis et al., 1983; Hyndman et al., 1997). The outer wedge is above the velocity-strengthening part of the subduction thrust, and the inner wedge overlies the velocity-weakening part. The velocity-weakening part is also known as the seismogenic zone (Scholz, 1998; Wang & Hu, 2006).

Dehydration processes play a major role in the rheological behavior of the basal thrust (e.g., Bachmann et al., 2009; Bilek & Lay, 1998; Byrne et al., 1988; Moore & Saffer, 2001; Saffer & Tobin, 2011). Large amounts of fluids are released due to compaction and diagenesis of the initially water-saturated sediments entering the subduction zone (Kastner et al., 1991; Moore & Vrolijk, 1992). Additionally, fluids are also set free by thermally driven dehydration reactions (Pytte & Reynolds, 1989; Vrolijk, 1990). These lithification processes cause the onset of velocity weakening by strengthening the hanging wall sediments, thereby facilitating rapid fault movement as consequence of seismic activity in the accretionary wedge (Dielforder et al., 2016; Fisher & Byrne, 1987; Moore & Saffer, 2001; Saffer & Tobin, 2011; Tobin & Saffer, 2009; Ujiie & Kimura, 2014).

There are several major fluid escape pathways in accretionary wedges. Fluids from underneath the plate interface, for example, in the underthrust sediments, are channeled along the basal shear zone (Maltman & Vannucchi, 2004; Moore & Vrolijk, 1992). Fluids generated from sediments within the deepest parts of the accretionary wedge generally move upwards along complex three-dimensional fault and fracture systems (Behrmann, 1991; Moore & Vrolijk, 1992; Saffer & Tobin, 2011). Typically, within this deep inner wedge, the intergranular permeability of the sediments is low, due to a porosity reduction via compaction and cementation (Akker et al., 2018; Dielforder et al., 2016; Moore & Vrolijk, 1992).

Studies on exhumed accretionary wedges and subduction mélanges, such as can be found in the Franciscan Complex in western North America (Meneghini & Moore, 2007), the Apennines in Italy (Meneghini et al., 2007; Vannucchi et al., 2010), the Chugach Mountains as well as Kodiak Island in Alaska (Fisher & Brantley, 2014) and the Shimanto Belt in SW Japan (Raimbourg et al., 2014), document the different types of deformation structures that allowed paleo-fluid transport. Macro-scale veins are common in exhumed wedges and typically show crack-seal textures that form at low temperatures (<150°C) (Boulton et al., 2022; Dielforder et al., 2015; Fagereng et al., 2010; Meneghini et al., 2007, 2009; Mittempergher et al., 2018; Palazzin et al., 2016; Raimbourg et al., 2019; Vannucchi et al., 2010). Such veins are treated as the record of fractures, which temporarily enhance permeability, allowing for fast fluid transport (Behrmann, 1991; Sibson et al., 1975). However, until now, there is little quantitative information on the link between micro-scale fluid collection and the spatial distribution of associated fluid pathways across different scales.

Therefore, this study aims at providing quantitative data on the spatial distribution of veins at various scales, including the micro-scale. We describe the geometrical aspects of fracturing and vein formation from field mapping to thin-section scale, delivering a time-integrated fracture data set of various degrees of opening and sealing from the kilometer to the micron-scale. We study the exhumed accretionary wedge in the Glarus Alps in eastern Switzerland, which documents the inversion of a foreland basin and emplacement of nappes (Herwegh et al., 2008; Pfiffner, 1986, 1993; Schmid et al., 1996). We use Synchrotron X-ray Fluorescence Microscopy (XFM) to visualize and quantify the dimensions and spatial density of micro-scale vein generations. Moreover, we document overprinting relationships between veins and the ductile deformation structures in the phyllosilicate-rich matrix, which provides insight in the link between cyclic brittle and viscous deformation. In addition, orientation data of veins and foliation lead to testable hypotheses related to the state of stress during fracturing and vein formation, allowing for a potential link and quantification with co- and inter-seismic stages in such highly deformed meta-sedimentary rocks at temperatures <330°C.

## 2. Geological Background

The European Alps result from the subduction of the Piemonte-Ligurian Ocean, Briançonnais swell and the Valais underneath the Adriatic plate, followed by the collision of the continental European and Adriatic plates (Dewey & Bird, 1970; Frisch, 1979; Handy et al., 2010; Musso Piantelli et al., 2022; Schmid et al., 2004, 2017). In the Eocene, just before the onset of continent-continent collision, the distal European margin entered the

subduction zone, which led to thickening of the upper plate and development of the underfilled North Alpine Foreland Basin. Within this basin, changes in both sediment catchment areas and depocenters with time, as well as the detailed mapped lithostratigraphy, allows the resulting Flysch Units to be subdivided in different units: the Ultrahelvetic, Southhelvetic and Northhelvetic Flysch Units (Lihou, 1996; Sinclair, 1997). In general, all these units comprise hemipelagic shales, marls, limestones and syn-orogenic turbidites (Dielforder et al., 2015, 2022; Sinclair, 1997). These sediments are of Upper Cretaceous to early Oligocene age (Lihou, 1995) and were accreted onto the orogenic Alpine wedge, metamorphosed and exhumed due to progressive convergence between the Adriatic and European plate. The Ultrahelvetic, Southhelvetic, and Northhelvetic Flysch Units were accreted onto each other in order of their paleogeographic deposition from south to north.

This geodynamic framework induced deformation within the sedimentary Flysch Units. The deformation has to be seen in a continuum of progressive shortening, but can locally be separated into different deformation phases (e.g., Gasser & Den Brok, 2008; Herwegh et al., 2008; Milnes & Pfiffner, 1977; Pfiffner et al., 2011). The continuum of deformation in space and time is evidenced by observations that soft-sediment deformation by particulate flow at the front of the outer wedge occurred synchronously with metamorphism and hard-sediment deformation in the inner wedge, overprinting the early deformation structures (Akker et al., 2021a; Dielforder et al., 2015, 2016, 2022). In the outer wedge, compaction and dehydration of the unconsolidated Flysch sediments present the first processes, followed by more pervasive non-coaxial deformation by particulate flow behavior (Dielforder et al., 2016). The diagenetic/metamorphic processes result in a gain in cohesion. At the large scale, north-vergent folds with steep axial planes and a dominant axial planar foliation as well as Flysch internal thrusts evolved. Earlier outer wedge deformation structures became largely overprinted by the younger pervasive inner wedge deformation but can locally still be found and identified by calcite veins and their Sr isotopes with marine signatures (Dielforder et al., 2015, 2016, 2022).

This prograde deformation from the outer to inner wedge is well recorded in the phyllosilicate-rich sediments by the evolution of a densely spaced foliation. This foliation accommodates strain by the thermally activated operation of pressure dissolution creep (Akker et al., 2021a). The reorganization of phyllosilicates into a densely spaced foliation is also well documented by the isotopic K-Ar system that shows along the prograde evolution: (a) an increase in amount of recrystallized phyllosilicates versus detrital grains, and (b) changes in the phyllosilicate chemistry (paragonite vs. pyrophyllite component) (Akker et al., 2021b). The progressive consolidation also increased the elastic moduli of the sediments, as is recorded by fracturing and the formation of calcite and calcite-quartz veins (Dielforder et al., 2015, 2016).

From a geodynamic point of view, the Glarus Flysch Units accreted during the late stage of subduction just prior to continent-continent collision. The framework therefore differs from a classical ocean-continent subduction, where the plate interface between subducting oceanic crust and continental upper crust is defined by a spatially restricted and clearly defined *mélange* zone. Instead, the tectonic framework is defined by a lower plate of thinned continental basement and overlying sediments of the Helvetic passive margin and an upper plate composed of sheared sediments of the Briançon swell and Valais trough. The active plate interface therefore consists of sediments in both the hanging and footwall. Still in a late subduction scenario, Flysch Units deformed directly underneath the plate interface, the latter being defined by the active Penninic basal thrust of the overlying nappe stack. The active basal thrust changed its position in space and time with progressive subduction, leading to successive accretion of the different Flysch Units mentioned above (Pfiffner, 1986). With the onset of continent-continent collision classical in-sequence thrusting was replaced by out-of-sequence thrusting by the famous Glarus thrust. This out-of-sequence thrust was active during peak and early retrograde metamorphic conditions (Badertscher & Burkhard, 2000; Badertscher et al., 2002; Ebert et al., 2007; Herwegh et al., 2008; Pfiffner, 1977; Schmid, 1975). For that reason, the Glarus thrust cut and decapitated the earlier active plate interfaces, which led to the preservation of the footwall Flysch Units only (e.g., Herwegh et al., 2008). As indicated by K-Ar data (Akker et al., 2021b), peak metamorphic conditions and associated deformation had some impact on deformation and recrystallization in Flysch units. In this sense, the Glarus thrust represents an important temporal marker because it truncates older accretion-related deformation structures in the underlying Flysch Units resulting from aforementioned stages of accretion. Activity of the Glarus thrust continued during retrograde conditions, leading to an offset of the peak metamorphic isogrades of about 10 km (Ebert et al., 2007; Groshong Jr et al., 1984; Rahn et al., 1995). In total, the Glarus thrust accommodated a displacement of 40–50 km within the Lochsite tectonites (Pfiffner, 1985). Considering such displacements, ductile deformation processes (Ebert et al., 2007; Schmid, 1975) alternated with brittle deformation and synkinematic veining, suggesting a substantial reduction of the effective stress by

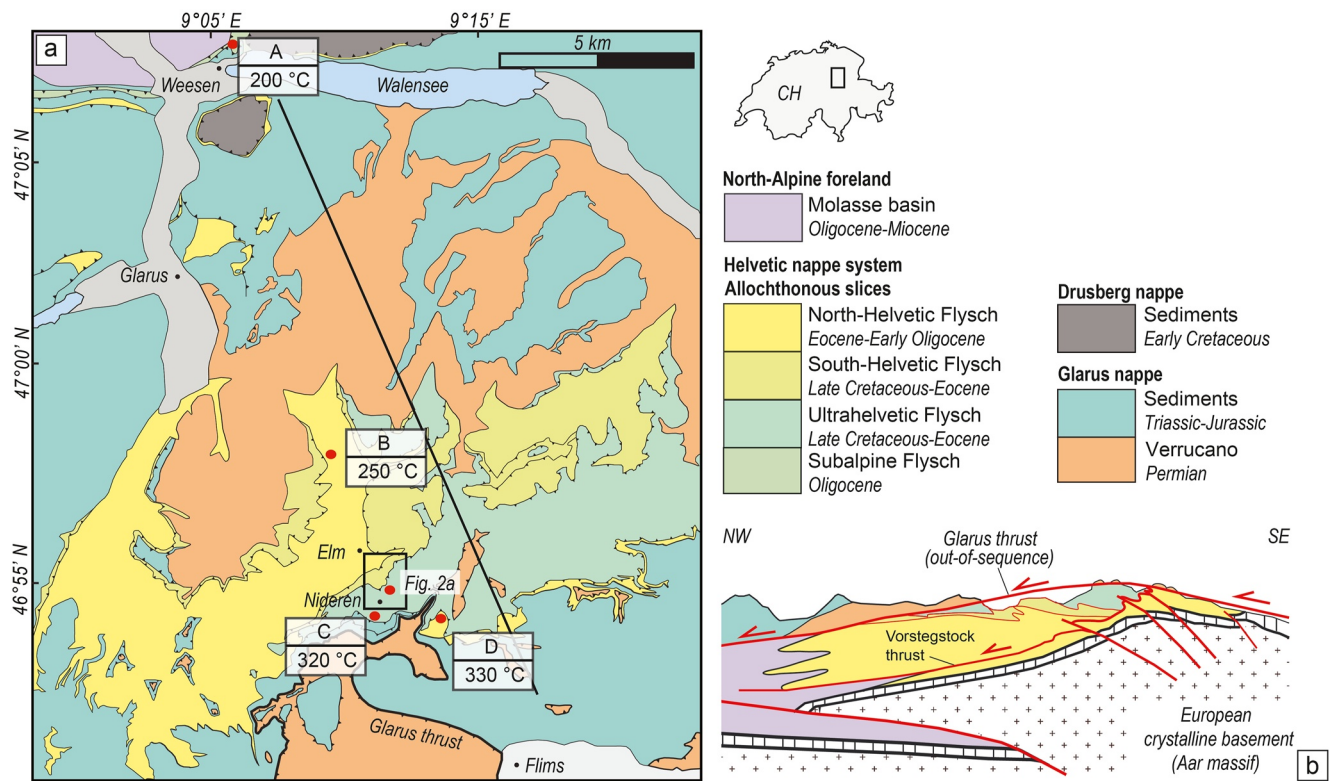


**Figure 1.** Geological map with sample locations and NW-SE tectonic cross section modified after Dielforder et al. (2016) and references therein. (a) Geological map with sample locations. Black box marks the area of the vein map in Figure 2a. Peak metamorphic temperatures are from Ebert et al. (2007), Lahfid et al. (2010), and Rahn et al. (1995). (b) Cross section along profile line in (a).

enhanced pore fluid pressures (Badertscher & Burkhard, 2000; Ebert et al., 2007; Herwegh et al., 2008; Poulet et al., 2014). The Flysch Units and their dehydration have been proposed as one major fluid source that reduced the effective stress by an increase in fluid pressure (Badertscher et al., 2002; Hürzeler & Abart, 2008). However, when, where, and by which processes this fluid liberation in the Flysch Units took place requires more quantitative investigations.

Uplift of the basement rocks of the Aar Massif resulted in a dome shape of the thrust plane and overlying nappe (Pfiffner et al., 2011; Schmid, 1975). Thrusting activity along the Glarus thrust must have occurred prior to this uplift, which resulted in the folding of the Glarus thrust and started at 22 Ma (Herwegh et al., 2020; Nibourel et al., 2021). Peak metamorphic conditions, show an increase in metamorphic grade in the Flysch Units from north to south (Figure 1). Peak metamorphic temperatures were established from calcite-dolomite thermometry (Ebert et al., 2007), Raman spectroscopy on carbonaceous material (Lahfid et al., 2010), and fluid inclusion data (Rahn et al., 1995) and show an increase from 200°C in the north (Weesen) to 330°C in the south (Segnespass).

### 3. Methodology

Metamorphic peak temperatures increase throughout the Flysch Units (North-, South- and Ultra-Helvetic Flysch) from north to south (Figure 1 and references therein). This sedimentary cover sequence reflects a time sequence in which all units were first in an outer wedge setting and then in an inner wedge setting (Dielforder et al., 2016). Key samples along this metamorphic gradient (Figure 1; Table 1) were selected (Akker, 2020). Sampling focuses on pure slate samples, excluding sand- and limestone-rich intervals in the sedimentary stratigraphy.

The studied slate units contain veins with varying spatial distribution. Veins either occur as individuals, clusters of few veins, and zones consisting of several tens to hundreds highly concentrated veins, referred to as vein-arrays in the following. To characterize the frequency, spatial distribution, and dimensions of vein-arrays, we mapped vein-arrays in a transect from the South to the Ultrahelvetic Flysch in the area between Elm and Nideren (Figure 1a). The mapped arrays occur in the Flysch Units below the Glarus thrust. From these vein-arrays, we



**Table 1**  
*Overview of Samples, Coordinates, Lithology, and Metamorphic Peak Temperatures*

| Sample ID | Sample name | Latitude     | Longitude   | Lithology                   | Metamorphic peak temperature (°C) |
|-----------|-------------|--------------|-------------|-----------------------------|-----------------------------------|
| A         | 16W01       | 47°08′26.3″N | 9°06′26.1″E | Slate                       | 200                               |
| B         | 17LP06      | 46°58′12.0″N | 9°09′19.7″E | Slate                       | 250                               |
| C         | 16MM01      | 46°53′29.0″N | 9°11′22.4″E | Calcareous slate            | 320                               |
| D         | 16SS01      | 46°53′02.8″N | 9°13′28.8″E | Slate                       | 330                               |
| E1/E1.1   | 17N1A/17N1B | 46°54′17.5″N | 9°12′11.3″E | Calcareous slate—vein-array | 300                               |
| E2        | 17N2        | 46°54′23.0″N | 9°12′04.2″E | Calcareous slate—vein-array | 300                               |
| E3        | 17N3        | 46°54′25.7″N | 9°12′01.7″E | Calcareous slate—vein-array | 300                               |

*Note.* The metamorphic peak temperatures are from Ebert et al. (2007), Lahfid et al. (2010), and Rahn et al. (1995).

sampled both the slate host rock as well as veins for microstructural and micro-chemical analyses. The samples presented in this study are from a series of neighboring vein-arrays at Tschinglen (Figure 2a and Table 1).

For the microstructural and chemical investigations, we combined light microscopy, scanning electron microscopy (SEM) and XFM. To estimate the foliation density and relative strain intensity of the slate samples, 2D autocorrelation functions are used (Akker et al., 2021a). Scan-line approaches are employed to measure width and spacing statistics for micron-veinlets in the XFM maps, as described in detail in Section 3.4.2.

### 3.1. Vein Mapping

Vein mapping was performed between Lauiboden in the north and Tschinglen in the south. This area is part of the UNESCO World Heritage Tectonic Arena Sardona (Figure 2a). The mapping area covers ~3 km<sup>2</sup> with a topography change from 1,000 m at Lauiboden to 1,700 m above Tschinglen. The foliation in the area dips consistently to the SE (strike 077°), which is also the average orientation of the bedding and the foliation-subparallel veins (Figure 2b). Considering the inclined bedding with respect to topography, the 2 km long transect represents about 1.5 km of true thickness of a wedge part of the Lower Helvetic Flysch Units (Figures 2b and 2c). Individual layer-parallel vein frequency and thicknesses were determined in the field.

Vein arrays including a series of densely spaced layer-parallel veins were mapped (Figure 2a) on the topographic map sheets on a scale of 1:2500 from Bundesamt für Landestopografie swisstopo. Orientations of bedding, foliation and veins (dip direction/dip) were plotted using Stereonet software 10.2.0 from Richard W. Allmendinger (Allmendinger et al., 2011; Cardozo & Allmendinger, 2013).

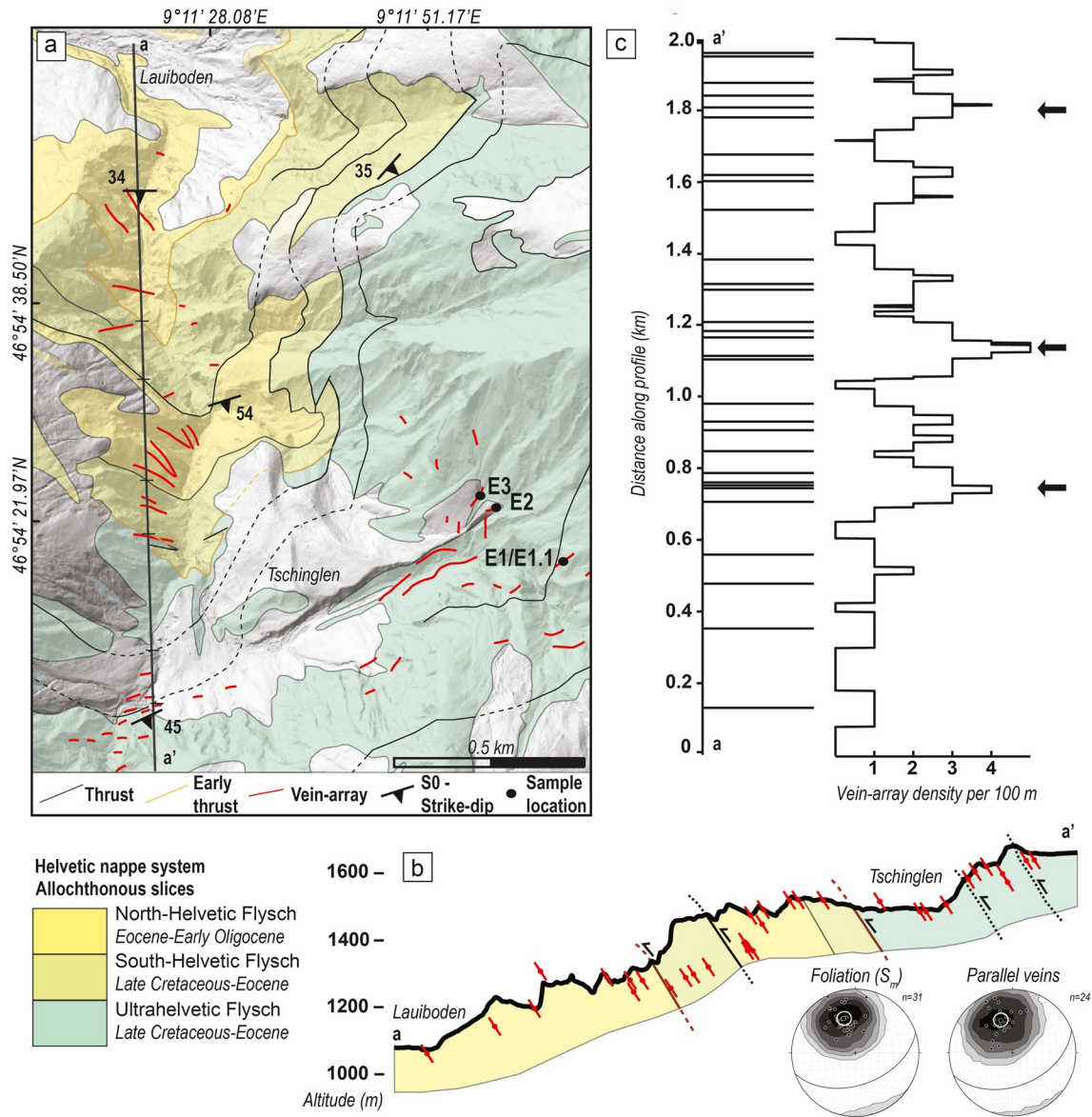
Vein-arrays mapped as red lines (Figure 2a) were projected along the average strike (077°) onto profile *a-a'* at their corresponding altitude (Figures 2a and 2b). The distances (perpendicular to the vein strike) between the vein-arrays are shown in Figure 2c. Vein array density was quantified with a moving-average calculation with a window size of 100 m using MATLAB® R2017b. Figure 2c shows the resulting vein-array frequency plot on the right-hand side.

### 3.2. Microstructural Imaging

Thin sections were cut from rocks perpendicular to the foliation, in all cases lineations were not observed. For microstructural imaging of thin sections, a Zeiss EVO 50 SEM with backscatter and secondary electron detectors was used at the Institute of Geological Sciences, University of Bern. Main operating conditions were 20 kV and 500–1,500 pA. Image mosaics were created with the photo-merging tool in Photoshop CS5.1.

### 3.3. Synchrotron X-Ray Fluorescence Microscopy (XFM)

Rocks were prepared for XFM analysis by thin sectioning on high-purity quartz slides without cover slips. All sections were imaged at the XFM beamline at the Australian Synchrotron (Howard et al., 2020), with an 18.5 keV X-ray beam focused by Kirkpatrick-Baez mirrors into a ~2 μm spot at the sample. Each specimen was scanned continuously with a scanning velocity of 2 mm s<sup>-1</sup> in the horizontal direction and a sampling interval in both the *x*- and *y*-direction of 2 μm, yielding a resolution of ~2 μm and an effective per-pixel dwell of 1 ms. Excited fluorescence photons were collected using a Maia (Rev D) detector system (Siddons et al., 2014) positioned in its



typical backscatter geometry. Spectra were deconvoluted using the Dynamic Analysis (Ryan & Jamieson, 1993) method implemented in GeoPIXE (Ryan et al., 2005) and quantified using known metallic foils, producing quantitative images of element distributions from sulfur to strontium.

3.4. Image Analysis

3.4.1. Fabric Analysis With 2D Auto-Correlation Functions (ACF)

2D ACF are a classic tool for the quantitative analysis of digital images of rock fabrics (Heilbronner, 2002; Heilbronner & Barrett, 2014). We used tessellations of ACF to estimate foliation orientation distributions and

strain-intensity estimates from our XFM maps. Since the foliation in our samples is defined by phyllosilicates (Akker et al., 2021a), Fe maps (elevated concentrations in chlorite) were employed to compute the foliation orientation distributions (Figure S1a in Supporting Information S1). The primary calcite of carbonate clasts in our calcareous slates is mainly composed of Globigerina fossils, which are agglomerates of spheres in their undeformed state. The remnant calcite skeletons of these fossils can survive to very high strains and are characterized by their high Sr concentrations. Hence, deformation-induced shape changes of the Globigerina were investigated by the use of XFM Sr maps to derive proxies for strain intensity with ACF tessellations (Figure S1d in Supporting Information S1).

For tessellation, the XFM maps were split into non-overlapping rectangular tiles with side lengths between 332 and 475 pixels corresponding to 664 and 950  $\mu\text{m}$  (Figure S1 in Supporting Information S1). For each tile, the ACF was computed and visualized in contour plots with 0.1 increments (Figures S1b and S1e in Supporting Information S1). The normalized ACF in each tile was thresholded at the 15%-level. The resulting binary image contains the cross-section of the central ACF peak at the 15%-level and occasionally those of secondary ACF peaks with correlations  $>15\%$  (Figures S1c and S1f in Supporting Information S1). In each tile, all thresholded particles were fit with an ellipse (inset of Figure S1a in Supporting Information S1). The long-axis orientation of the best-fit ellipse serves as a proxy for local foliation orientation. Long-axis frequency distributions were visualized in polar plots. The aspect ratio of the best-fit ellipse is defined as long axis/short axis. In each processed ACF tile of the Sr maps the aspect ratio was employed as a local strain proxy. Aspect-ratio frequency distributions were visualized in histograms. All analyses were carried out with MATLAB® R2017b.

### 3.4.2. Vein-Spacing and -Width Statistics for Micron-Veinlets

Micron-veinlets are veins with a thickness of about 10 microns. We employed slightly different strategies for analyzing the orientation, spacing and width of micron-veinlets that occur in the slate matrix versus those that are preserved within foliation-parallel veins.

To obtain spacing and width statistics of micron-veinlets in slate, XFM maps were analyzed. Compared to Ca K- $\alpha$  photons, Sr K- $\alpha$  photons have a greater escape depth (approximately 10 and 300  $\mu\text{m}$  respectively), allowing sampling of Sr through the entire thin section. Furthermore, at the incident energy of 18.5 keV, Sr has approximately an order of magnitude higher absorption cross section, resulting in a higher detectable fluorescent yield and therefore a higher fidelity signal (Henke et al., 1993). Since the examined micron-veinlets contain Sr-rich calcite, we employed XFM maps of Sr for spacing analysis. Because all maps of interest also contain Sr-rich foliation-parallel veins, they are cropped into sections without such parallel veins. The resulting map sections are rotated such that the micron-veinlets assume, on average, a vertical orientation with respect to the image (Figure S2a in Supporting Information S1). Then, horizontal Sr scan lines were extracted with vertical distances between 10 and 30 pixels (Figure S2c in Supporting Information S1). On each scan line, vein positions were defined as the positions of peaks in the Sr profile with a certain minimum height above the background signal (Figure S2c in Supporting Information S1) and a minimum peak prominence of 10  $\mu\text{g}/\text{cm}^2$ . Vein aperture is defined as the full-width at half-maximum (FWHM) of each peak. Finally, the scan-line results of all sections were combined for each sample. Their frequency distributions were visualized with box-and-whisker plots. These analyses were carried out with MATLAB® R2017b.

In the case of micron-veinlets within foliation-parallel veins (Figure S3 in Supporting Information S1), quantification of veinlet spacing and width is similar to the aforementioned strategy (Figure S2 in Supporting Information S1) with one fundamental difference: the distances and lengths of individual scan lines perpendicular to the veinlets were chosen manually. This is necessary because the foliation-parallel host veins are also rich in Sr and thus contain areas where it is difficult to recognize the micron-veinlets based solely on their Sr concentration. Moreover, the host veins also experience replacement of calcite by quartz postdating the emplacement of veinlets (Figure S3a in Supporting Information S1). In such areas, veinlets were wiped out locally, which in turn caused a measurement error in scan lines traversing such zones. Therefore, manual selection of areas of interest was employed to guarantee high fidelity in the measurements. The relevant parameters for geometric analysis of veinlets within foliation-parallel veins are listed in Figure S3e of the Supporting Information S1. The spacing and width distributions are shown in Figures S3c and S3d of the Supporting Information S1, respectively.

## 4. Results

### 4.1. Large-Scale Vein Distribution and Their Relative Timing

Each of the different Flysch Units comprises distinct sedimentary strata of alternating slates, limestones and sandstones. South of Lauiboden (Figure 2), slates are the most common lithology. The entire rock package is characterized by a secondary main foliation ( $S_m$ ), indicating an average steep to moderate dip to the southeast, with an average dip direction/dip angle of 161/48 (Figure 2b).

Within these slates, clusters of veins are observed, to which we refer to as vein-arrays (Figures 3a–3d). These arrays consist of an accumulation of individual veins. Individual veins have thicknesses in the 0.2–20 cm range, and lateral extents up to a few meters. Geometrically, we identify three vein families for which we establish the relative timing through crosscutting relationships: (a) folded veins (Figure 3e), which are crosscut by both (b) veins sub-parallel to  $S_m$  (hereafter referred to as “parallel” veins, Figures 3e, 3f, 4a, and 4c) and (c) “steep” veins sub-perpendicular to  $S_m$  (Figures 3f, 4a, and 4c). There is a mutual overprint relationship between “parallel veins” and “steep veins” (Figures 4a and 4c).

Vein-arrays are common in the highly strained slate layers south of Elm (Figures 1, 2, and 3a–3d). The vein-arrays vary between 1 and 20 m in width and continue along strike all the way through an outcrop. Hence, vein-arrays could be much longer than the vein map implies (Figure 2a). The average spacing between individual vein-arrays is about 50–100 m. The moving average calculation along the profile (Figure 2c) shows that the vein-arrays are concentrated in three main clusters. Two clusters are located just north of Nideren in the Ultrahelvetic slates, the other cluster is just at the boundary from the Ultrahelvetic slates to the overlying Ultrahelvetic carbonates. The spacing between the three clusters is ~400 and ~700 m.

### 4.2. Macroscopic Vein Types

Folded calcite veins occur with a wide range of orientations, from an angle of 80° to (sub)-parallel to the  $S_m$  foliation. Their spatial frequency is low. They usually occur as a single (Figure 3e) or a few folded veins (Figure 4a) together. However, there might be some observation bias at the outcrop scale. Folded veins that are sheared into parallelism with the foliation will become unfolded and therefore might be overlooked. The folded veins are in the range of 1 mm–1 cm thick and are strongly reworked in the host rock matrix (Figures 4a and 4c). This “reworking process” includes progressive shearing that leads to the rotation of the veins into the foliation as well as possible boudinage. Therefore, the internal texture of the veins does not always preserve the original emplacement texture.

The parallel veins are most common and make up the bulk of the vein-arrays (Figures 3b–3d, and 4a). Macroscopically measured parallel veins show orientations similar to the foliation, on average dipping steeply to moderately to the southeast (mean 159/46, Figure 2b). The parallel veins often crosscut the folded veins, but not exclusively (Figure 3e). These parallel veins show a wide variety of thicknesses between ~50  $\mu\text{m}$  and ~20 cm. Parallel veins have a blocky texture and consist mostly of calcite, with minor appearances of quartz. Black seams, of thicknesses up to 500  $\mu\text{m}$ , of phyllosilicates parallel to the  $S_m$  foliation intersect the veins (Figure 4b).

There seem to exist two sets of parallel vein geometries. One set is composed of vein widths in the mm to submillimeter range and lengths of several meters with tabular appearance in 3D space (Figures 3d and 4). The second set shows thicknesses in the cm to dm range and lengths from dm to several meters with lentoid shapes (Figure 3f, red arrow). Hence, the first and second set show “high” and “low” axial ratio (AR) geometries, respectively. We need to state already at this stage that we cannot rule out that some high-AR veins may represent highly stretched older low-AR veins. As will be presented below, however, there is clear evidence that many of the high-AR veins are emplaced as shear veins, characterized by a high AR at the time of formation. The low-AR set often forms along steps linking shear veins, producing pull apart domains (see Figure 3e just above “folded vein,” see also G2 veins of Dielforder et al. (2015, 2016)). However, we cannot rule out that some of them may also have evolved as mode-I fractures. In terms of frequency, high-AR veins are more common than the low-AR ones.

The steep veins cut the foliation at angles >30° and show high spatial frequency in recurring cm-wide domains (Figures 3f and 4a). The width of these calcite veins varies between 80  $\mu\text{m}$  (in thin sections) to 0.5 cm (in outcrops), and they crosscut both the folded and parallel vein types. However, steep veins get themselves also dissected by layer-parallel veins (Figure 4c).



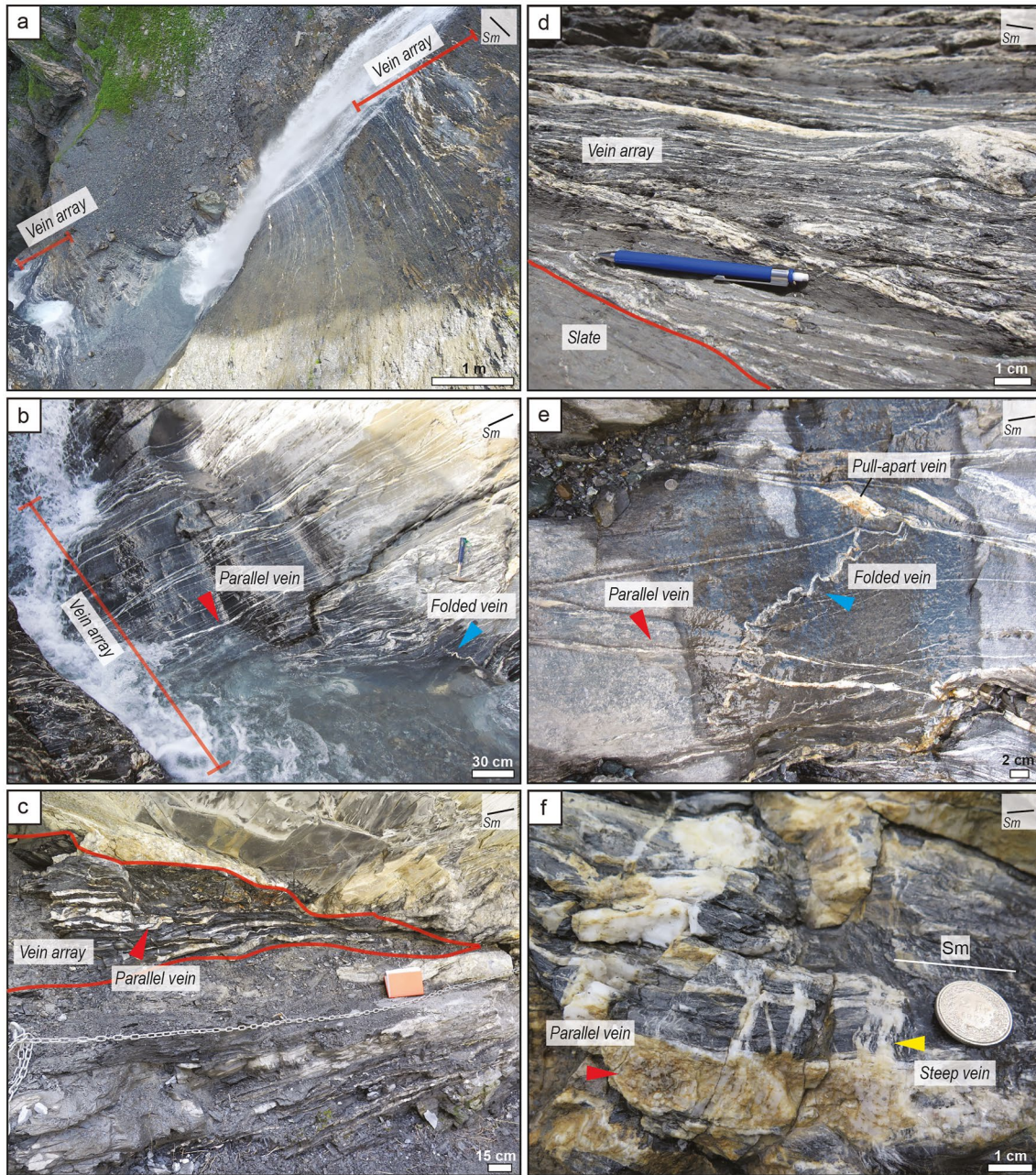


**Figure 3.** Vein macro-structures in the research area. (a) Down cliff view of vein-arrays parallel to the bedding which are repetitive and separated by slate domains without vein-arrays. (b) The vein-arrays mostly comprise parallel veins overprinting some minor folded veins. (c) Parallel veins making up vein-arrays have thicknesses up to 20 cm. (d) Vein-arrays also comprise parallel veins with thicknesses < 1 cm. (e) Folded veins, with a high angle to the bedding, are in many cases crosscut by parallel veins. In some cases, these parallel veins develop as pull-apart shear veins. (f) Parallel veins (red arrow) are crosscut by steep veins (yellow arrow).  $S_m$  marks the main foliation.

### 4.3. Vein Microstructures

#### 4.3.1. Parallel Veins

The internal Sr distribution of the studied parallel veins unveils coarse-grained blocky textures with growth zonation preserved in the thicker parallel veins (Figure 5a). The growth zonation is invisible with transmitted-light and electron-beam microscopy (e.g., see SEM BSE image in Figure 5c). The XFM-Sr map also reveals multiple generations of steep micron-veinlets preserved within parallel veins thicker than ca. 100  $\mu\text{m}$  (Figure 5a). Thin phyllosilicate seams parallel to the slate foliation cut the vein calcite, as evidenced by truncation of the growth



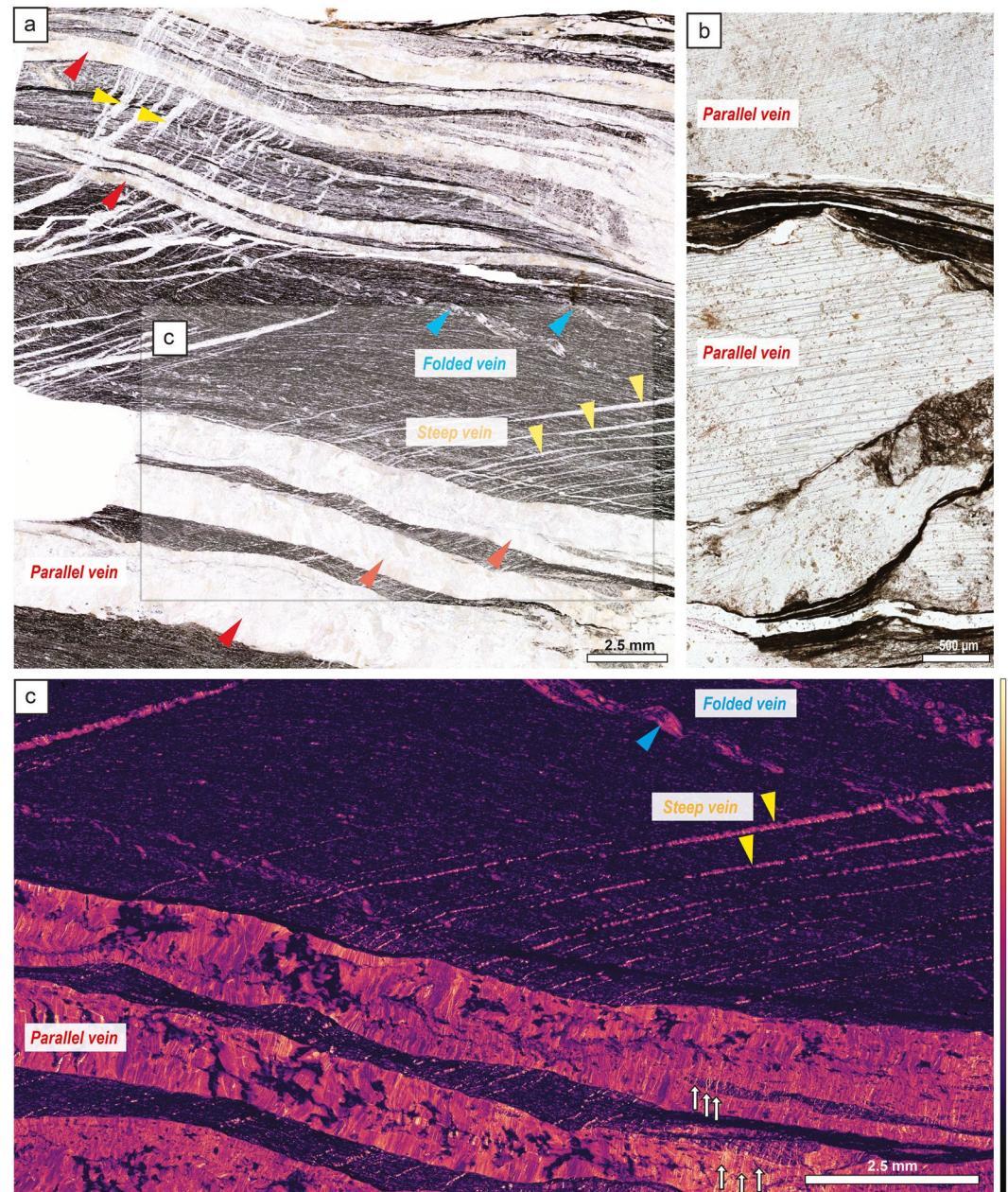


**Figure 4.** Optical light micrograph and XFM-Sr map showing three main vein types and overprinting relationships. (a) Thin section overview showing crosscutting relationships between three main vein types. Box indicates the location of the XFM map in (c). Folded veins (blue arrows) are overprinted by steep veins. Steep veins (yellow arrows) both dissect layer-parallel veins (red arrows; see upper left corner) as well get dissected by layer-parallel veins (red arrows; see lower right corner), also see XFM map in (c). (b) Black seams, made up of phyllosilicates, intersect coarse-grained blocky parallel veins (thicknesses > 1 mm). (c) XFM-Sr map (black to yellow shows low to high Sr concentrations) shows that steep veins (yellow arrows) are indeed dissected by layer-parallel veins. All images from sample E1.

zonation. Calcite veins often show a chlorite rim (Figures 5b and 5c). This rim is well visible in the XFM-Fe map due to the high Fe concentration within chlorite (Figure 5b).

#### 4.3.2. Steep Veins

Internal mapping of calcite veins with XFM reveals steep veins (thicknesses of about 10 μm) that occur as micron-veinlets at high angles to foliation (most commonly >60° but as low as 30°) that show a stripy Sr distribution (Figures 5–8) and were previously unseen in optical light and backscatter electron (BSE) micrographs



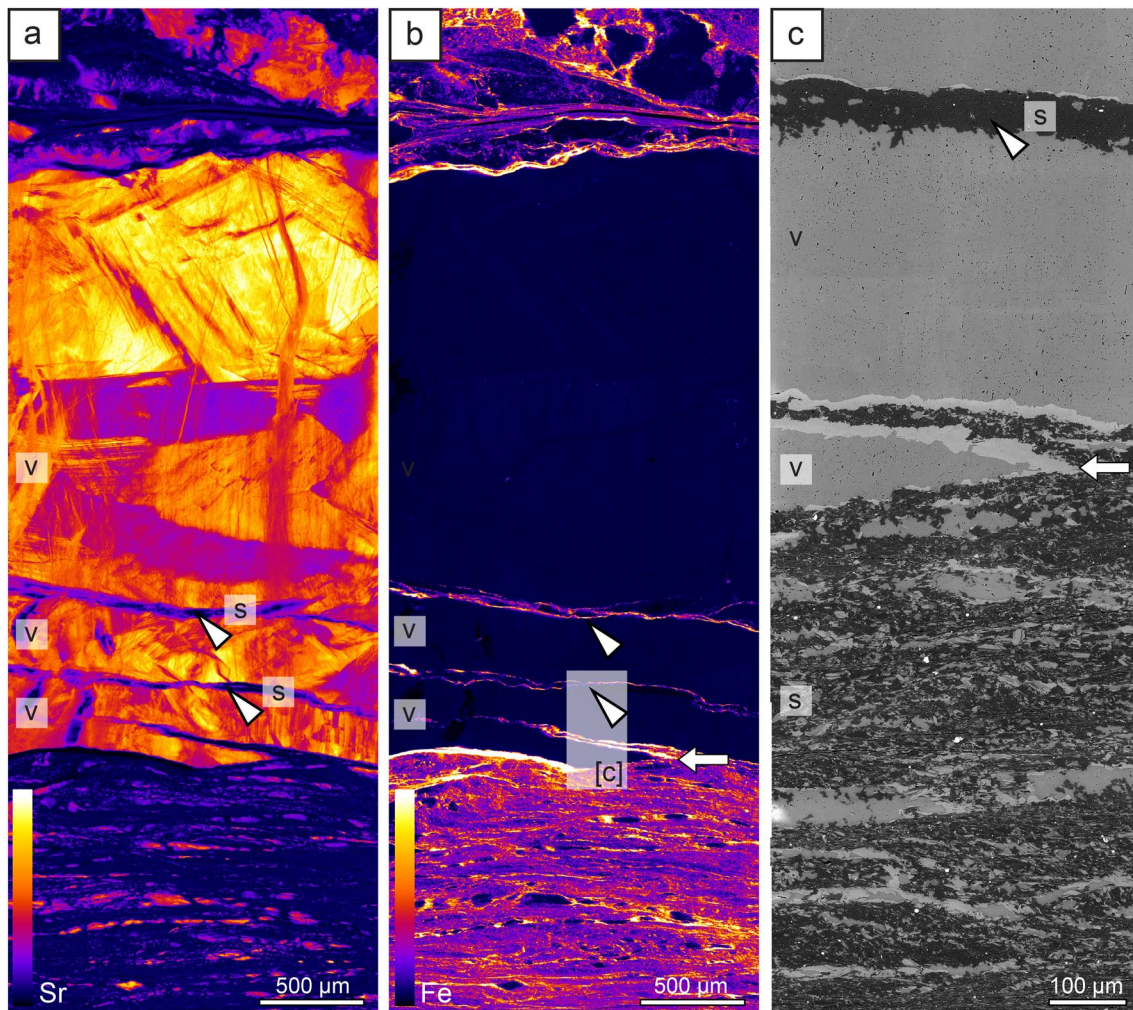


**Figure 5.** Internal growth zonation in parallel blocky veins in sample E1. (a) XFM-Sr map. The concentration from low (black) to high (white) is shown in the color bar. The slates contain phyllosilicate-rich domains: “s” with white arrowheads and vein domains: “v.” (b) XFM-Fe map and respective (c) BSE image, from the shaded region indicated in (b) and marked with a white arrow. The white regions around the calcite vein domain (V) are chlorite.

(Figure 5c). All studied calcite micron-veinlets show higher Sr concentrations relative to the matrix calcite (Figures 5–7). The micron-veinlets, like the steep veins described above, dissect the slate matrix (Figure 6) as well as parallel veins (Figures 4c, 5a, and 7) and crosscut other micron-veinlets (Figure 6). The micron-veinlets themselves are also overprinted by the slate matrix, indicating a mutual overprint.

Scan-line analysis shows that the micron-veinlets crosscutting the slate matrix are pervasively distributed (spacing of about 100  $\mu\text{m}$ ) and very thin (7–15  $\mu\text{m}$ ; Figure 6d; Figure S2 in Supporting Information S1). Micron-veinlets preserved within parallel veins (Figure 7) show a median spacing of 60  $\mu\text{m}$ . The median width of such veinlets is 12  $\mu\text{m}$  and thus similar to those within the slate (Figure 6; Figure S3 in Supporting Information S1).

Due to resolution limits, only the internal texture of steep micron-veinlets with thicknesses of  $\sim 100 \mu\text{m}$  could be imaged with XFM. They reveal an internal Sr zonation parallel to the veinlet walls (Figure 8a). In samples where calcite-rich layers alternate with phyllosilicate-rich layers on the micro-scale, micron-veinlets are best visualized in the calcite-rich layers (Figure 8a). Two end-member textures are observed within such micron-veinlets (Figure 8b): alternating planar zones of high and low Sr concentration, and patterns with a maximum Sr concentration in the veinlet center flanked by a symmetric gradual Sr decrease toward the margins.



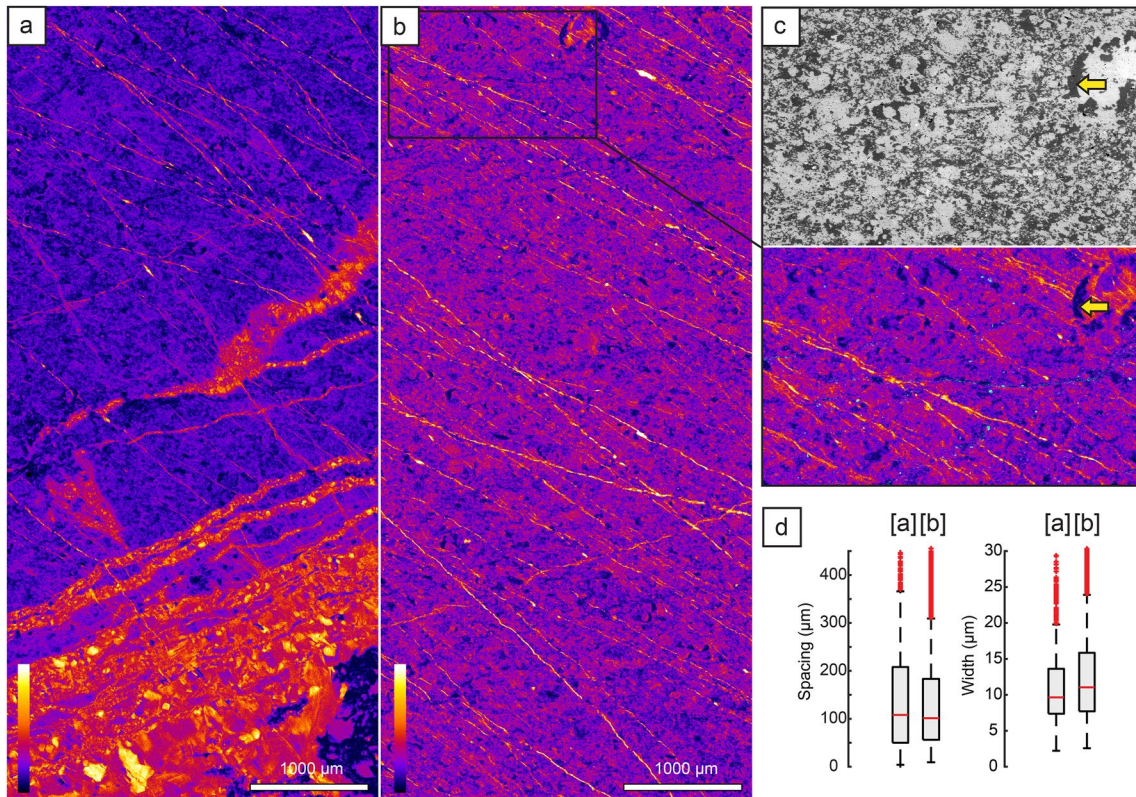


**Figure 6.** Micron-veinlets dissecting parallel vein and slate matrix in sample E2. (a and b) Sr maps (the concentration from low (black) to high (white) is shown in the color bar) show micron-veinlets that crosscut parallel veins with blocky texture (lower part in a) and slate matrix, in which they are pervasively distributed. (c) On SEM BSE images (top), micron-veinlets are not visible but appear in Sr maps (bottom). (d) Box-and-whisker plots showing vein spacing and width of micron-veinlets in matrix in (a) and (b).

#### 4.4. Ductile—Viscous Deformation

The slate matrix shows two main fabric elements: clasts, including detrital quartz, calcite and microfossils, and foliation planes made up by the aligned platy phyllosilicates. To visualize phyllosilicates, Fe and Ti are good markers because these trace elements are enriched within phyllosilicates, which define the foliation planes (Figures 9a–9c). With increasing metamorphic grade: (a) the foliation intensity in the slates increases as indicated by a decrease in foliation spacing, (b) the orientation of the foliation changes from an inclined angle of about 30° to almost parallel to the bedding (Figure 9d) and (c) the calculated ACF aspect ratios, which are a proxy for finite strain, indicate increasing strain levels (Figure 9d), as shown by Akker et al. (2021a).

XFM data confirm that the slate foliation forms by a combination of stress-controlled dissolution-(re)precipitation of phyllosilicates, dissolution of fossils, detrital calcite, and quartz clasts, precipitation of chlorite in their pressure shadows as well as rotation of detrital phyllosilicates in the foliation plane. These observations suggest local mass transfer processes by diffusive transport (e.g., Akker et al., 2021a).

The mutual overprint between steep micron-veinlets and the  $S_m$ -foliation is readily ascertained from the XFM map, shown in Figure 9e, which features two ca. 70 μm-thick steep veinlets crosscutting the slate matrix. Both veinlets have the same orientation within a ~1 mm-thick quartz-rich layer at the top of the image where they are about perpendicular to  $S_m$ . Within mica-rich domains, the right-hand vein is sheared dextrally with a bulk shear angle of ca. 45°. In contrast, the micron-veinlet on the left displays negligible shearing within the mica-rich layer and could be the result of a lower degree of dissolution associated with the associated smaller shear displacement compared to the right-hand vein. Interestingly, the wiggly margins of this poorly sheared vein potentially indicate micro-folding due to the shortening component of the overall non-coaxial strain field (normal to  $S_m$ ). It is also worth noting that the highly sheared veinlet on the right forms asymmetric local boudins (the white arrows indicate boudin necks). One can envisage how further shearing would have led to dissection of the



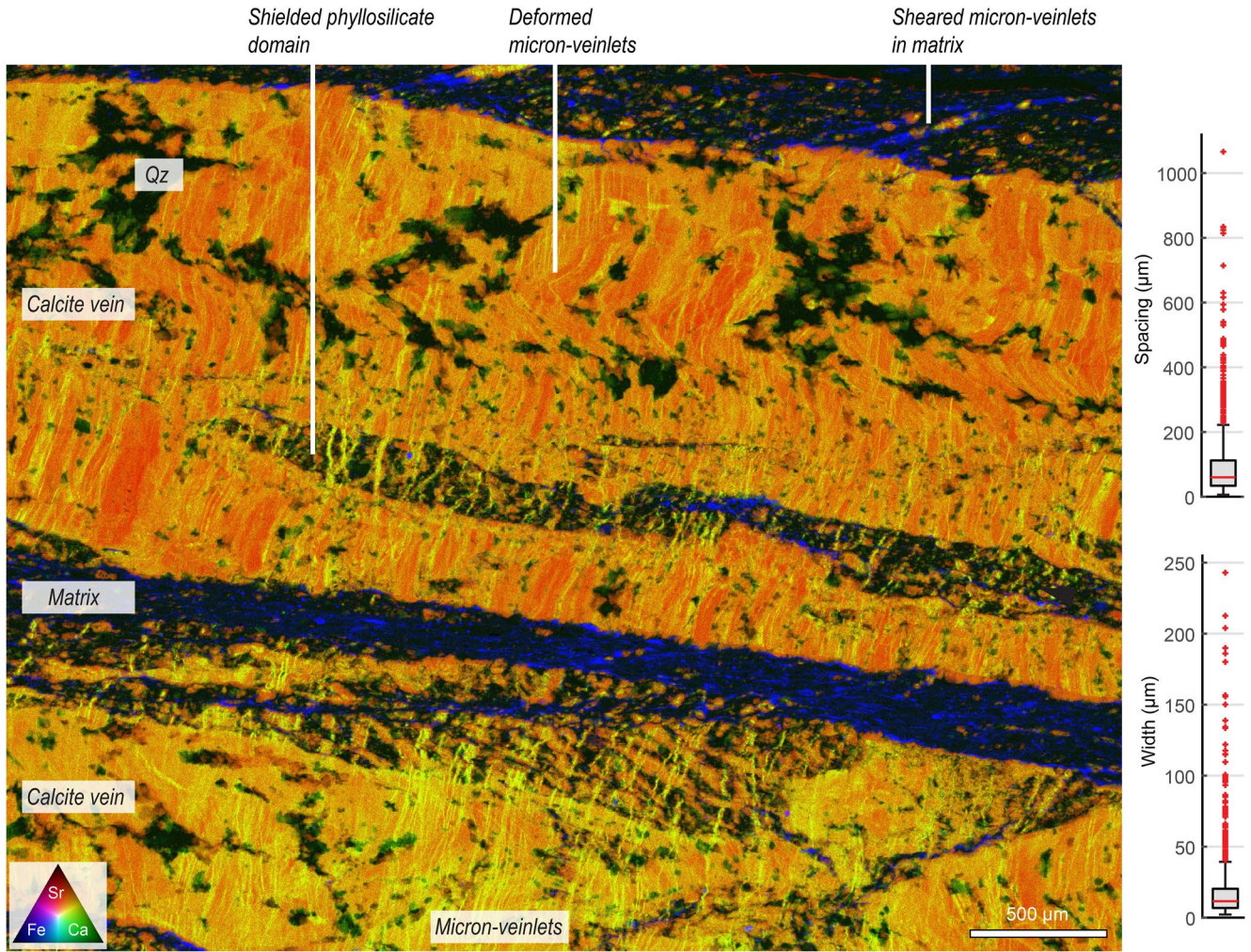


**Figure 7.** XFM map showing micron-veinlets dissecting a parallel calcite vein in sample E3 (Sr, Ca, and Fe shown according to the color triangle). A stripy texture is evident in red and orange with micron-veinlets in yellow. Micron-veinlets are in parts sheared within the matrix (blue linear features in upper right corner), are bent within the parallel vein and are shielded from dissolution in the phyllosilicate-rich domains within the parallel veins. Spacing and width statistics for micron-veinlets shown in box-and-whisker plots on the right side.

vein into  $\sim 50 \mu\text{m}$ -thick, asymmetric calcite grains, as seen so commonly in the surrounding slate matrix (see also Figure 9f). Eventually, due to ongoing non-coaxial deformation accommodated by pressure-dissolution creep, the micron-veinlets are completely transposed into small calcite clasts embedded into the phyllosilicate layers (Figures 7 and 9f), unless they are shielded within parallel coarse-grained calcite veins (Figure 7). Micro-folding and shearing of veinlets are also seen in micron-veinlets preserved within parallel veins (Figure 7). Another example of the progressive incorporation of micron-veinlets into the foliation is seen in Figure 9f, which shows highly transposed isoclinally folded veinlets. The veinlets are boudinaged, resulting in isolated calcite clasts and secondary phyllosilicates (mostly chlorite) precipitated in the necks of the vein-derived boudinaged fold limbs.

## 5. Discussion

In the present study, we document two sets of veins: (a) foliation-parallel calcite veins that form vein-arrays (meters thick, Figure 10), as well as (b) steep calcite veins including steep micron-veinlets with very high spatial densities (Figure 10). Over geological times ranging from outer to inner wedge deformation, vein-arrays accumulated different vein generations over time. These veins are studied in detail by Dielforder et al. (2015, 2016, 2022), who differentiated three vein generations, G1, G2, and G3. Vein emplacement temperatures for the oldest, foliation-parallel G1 veins obtained by Sr and O isotope studies range from 40 to 70°C, consistent with formation



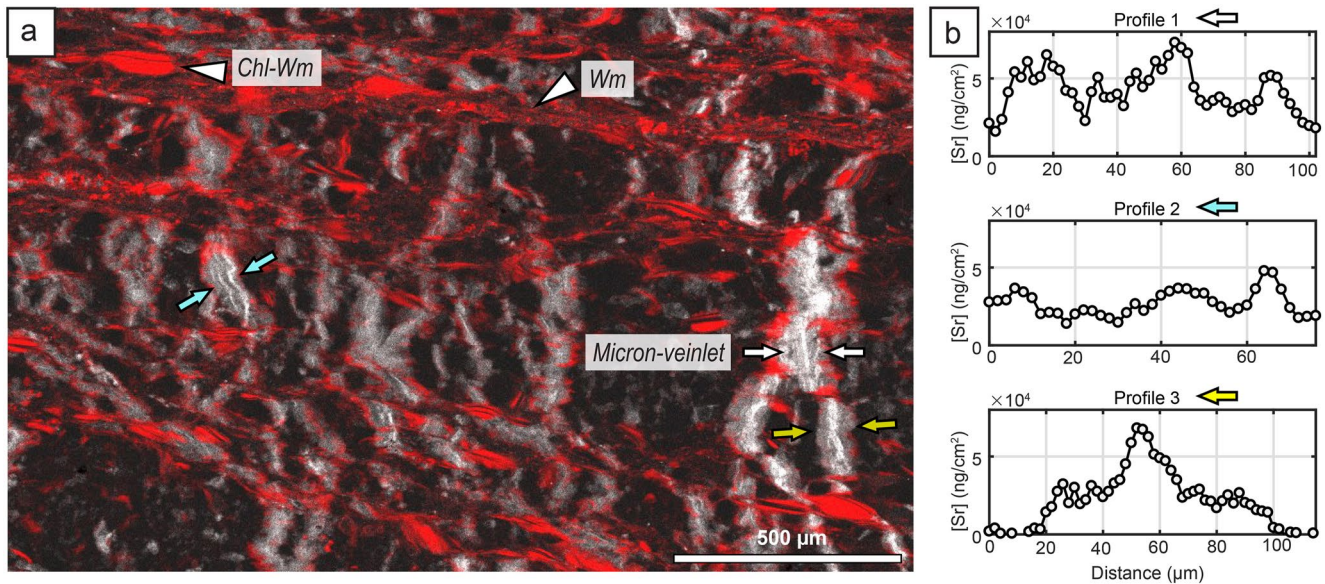


**Figure 8.** Internal Sr textures of steep veinlets (100  $\mu\text{m}$  width) within dark calcite-rich layers in sample E1.1 (gray is Sr, red is Fe). (a) XFM map shows alternation of phyllosilicate-rich layers (Wm) including chlorite-white mica (Chl-Wm) detrital phyllosilicates with calcite-rich layers. The micron-veinlets accumulated in the calcite-rich layers and show an internal Sr zonation parallel to the vein wall. (b) Profiles perpendicular to the micron veinlets (indicated with arrows in (a)) show two end-member textures: alternating zones of high and low Sr concentrations and patterns with maximum Sr concentration in the veinlet center flanked by a symmetric gradual Sr decrease toward the margins.

during early stages in the outer wedge (Dielforder et al., 2015, 2016, 2022). Younger G2 and G3 veins develop, respectively, parallel and perpendicular to foliation within the inner wedge, as indicated by increased emplacement temperatures (210–290°C) and structural overprinting (Dielforder et al., 2015, 2016, 2022). However, for the studied layer-parallel veins making up the vein arrays, we cannot always distinguish between G1 and G2 types without isotopic or structural evidence. In other words, some layer-parallel veins described here could either be inherited, potentially reactivated G1 veins or newly formed G2 veins. Nevertheless, our micrographs clearly contain some layer-parallel veins that formed at high temperature in the inner wedge, corresponding to G2 of Dielforder et al. (2015, 2016, 2022), as indicated by structural overprinting relationships (e.g., Figures 4 and 11). In the following, we discuss the multiscale architecture of fluid pathways, where and when in the wedge the veins formed and under what states of stress, the controls on the formation, location, and preservation potential of veins and vein-arrays and the implications for paleo fluid transport. Finally, we discuss how structures in the paleo-wedge could possibly be linked to seismic activity in active wedges.

### 5.1. Multiscale Architecture of Fluid Pathways in an Accretionary Wedge

Fractures and their interconnected fracture porosities indicate transient times of enhanced permeability (e.g., Cox et al., 1987). In the case of exhumed wedges, such as in the Glarus Alps, open fracture porosity did not prevail but was filled by precipitates. Hence, resulting veins provide records of paleo-fluid pathways. Our quantitative study on the spatial multiscale distribution of veins allows to share new light on the pathway architecture, which consists of two preferential orientations: (a) layer (bedding/foliation)-parallel and (b) layer-perpendicular ones (Figure 10a). The “steep” veins seem to be isolated but evenly distributed throughout the wedge and are much less frequent than the layer-parallel veins. Our XFM maps reveal the presence of micron-veinlets with spacing  $\leq 100 \mu\text{m}$ . Particular when being associated with layer-parallel veins, keeping in mind that we only examined samples from vein arrays, these densely spaced micron-veinlets constitute a pervasive micro-fracture network that enabled layer/foliation-perpendicular fluid transport. Note that in contrast to the cm- to dm-wide isolated G1 and G2 veins treated by Dielforder et al. (2015, 2016, 2022) the layer-parallel veins of our study appear in layer-parallel vein arrays and vein array clusters, respectively, with characteristic spacings of 50–100 m and 400–700 m (Figures 2c and 10a). Hence, they indicate a time-integrated accumulation of layer-parallel fluid transport channelized at least at three scales. In the following, we discuss the hydro-mechanical origin of the individual vein sets as well as their relevance for fluid transport in an evolving accretionary prism.



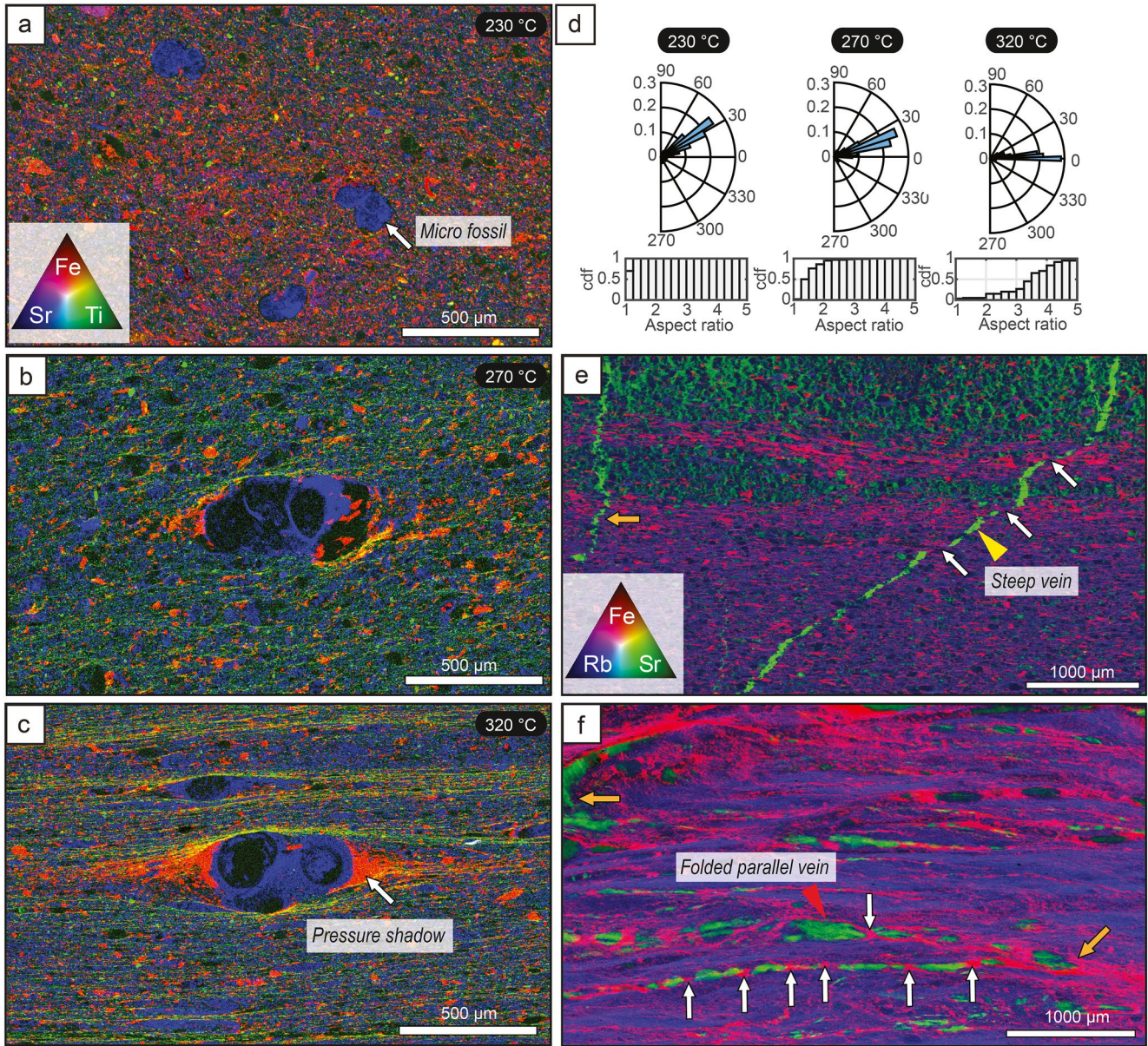


**Figure 9.** Deformation in slate matrix imaged with XFM. (a–c) Microstructural changes in slates with increasing temperature/strain (Fe, Sr, Ti shown according to the color triangle in (a); top to right sense of shear). The large circular calcite fragments are fossils. Note how the *Globigerina* chambers in the large fossil clast in (c) retain their circular shape and are truncated by the newly formed Ti-rich foliation on the high-stress sides of the clast. (a) is sample A, (b) is sample B and (c) is sample C. (d) Polar plots showing orientation of foliation relative to the main bedding and bottom diagrams represent ACF aspect ratios, the latter are an indicator for strain intensity. (e) XFM map showing Fe, Rb, Sr according to the color triangle. A steep vein emerges from the upper right corner of the map (yellow arrowhead) and then traverses the map obliquely to the lower left of the image. This vein is overprinted by secondary phyllosilicates (white arrows). The orange arrow points to a small micron-veinlet that lacks any signs of shearing and is thus interpreted to be younger than its sheared counterpart. Note that both steep veinlets exhibit a similar orientation within the quartz-rich layers (Fe-poor and thus appearing in green and black) (f) XFM map showing Fe, Rb, Sr according to the color triangle. Folded parallel vein with fold hinges (orange arrows). Chlorite precipitates in the necks of the boudins within the limbs of the transposed isoclinal folds (white arrows).  $S_m$  foliation in (a–c) and (e, f) is approximately horizontal. Images in (e) and (f) are sample D.

## 5.2. Where and When in the Wedge did Parallel and Steep Veins Form?

Our outcrop- and microscale observations (Figures 3f and 4–7) clearly demonstrate that both vein orientation families and the secondary spaced foliation (slate foliation) within the host rock overprint each other mutually and thus formed during the same progressive deformation. Dating of secondary phyllosilicates making up the slate foliation yields maximum deformation ages in the range of 30–27 Ma (Akker et al., 2021b), showing that



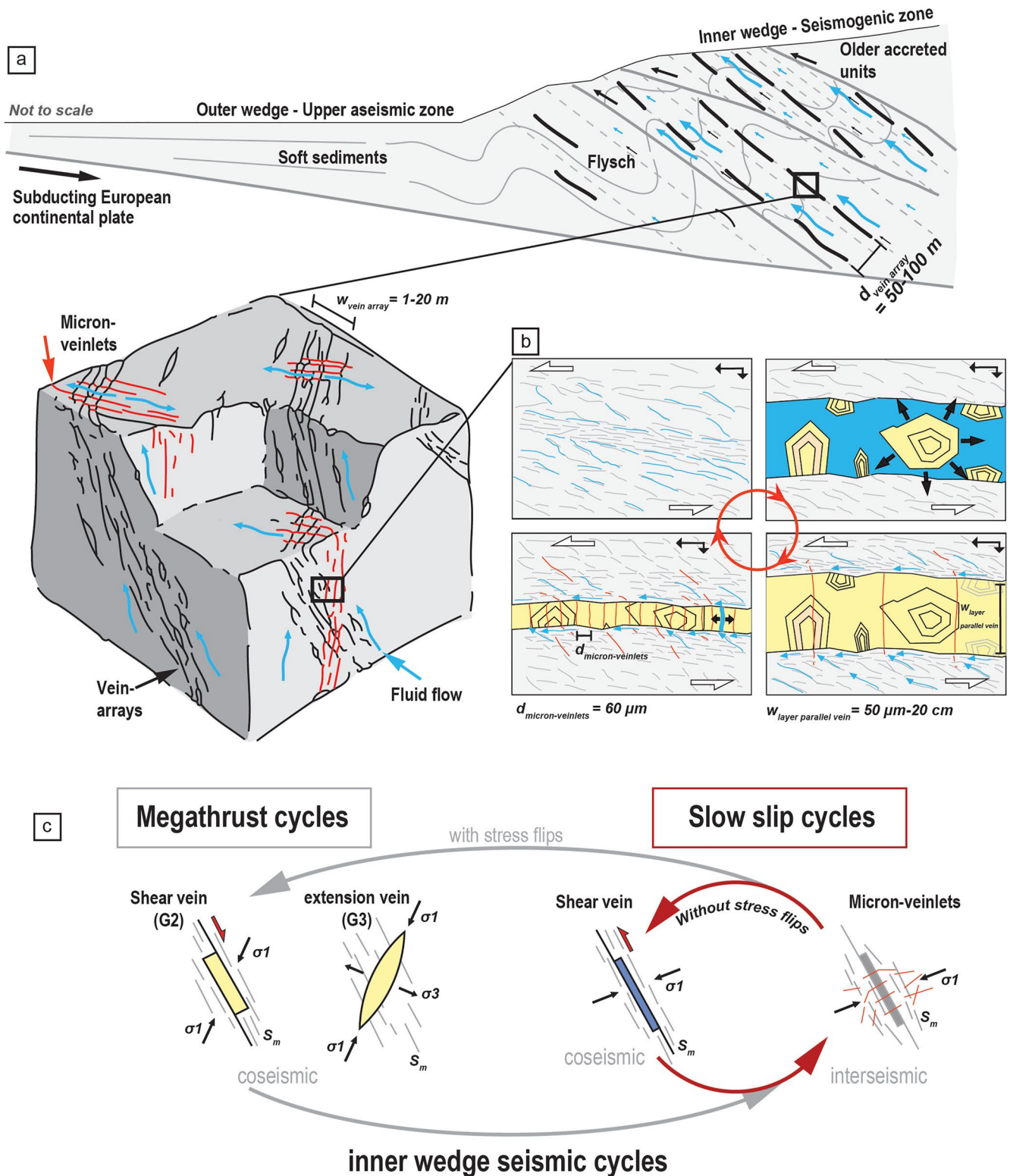


**Figure 10.** Mutual overprint of all deformation structures in the inner wedge. (a) The upper part shows the accretionary wedge with vein-arrays (black lines) subparallel to the Flysch internal thrusts (sketch of this wedge after Dielforder et al. (2016)). The block diagram shows the vein-arrays in relation to the micron-veinlets, documenting an upwards as well as horizontal fluid transport. (b) Interpretation of microscale deformation, linking slate internal deformation and repetitive fracturing as a function of increasing strain for the same location. (c) Conceptual model to link slow slip and megathrust earthquake cycles with aseismic background deformation. Slow slip cycles with layer-parallel veins and micron-veinlets based on results of this study, megathrust cycle based on Dielforder et al. (2015).



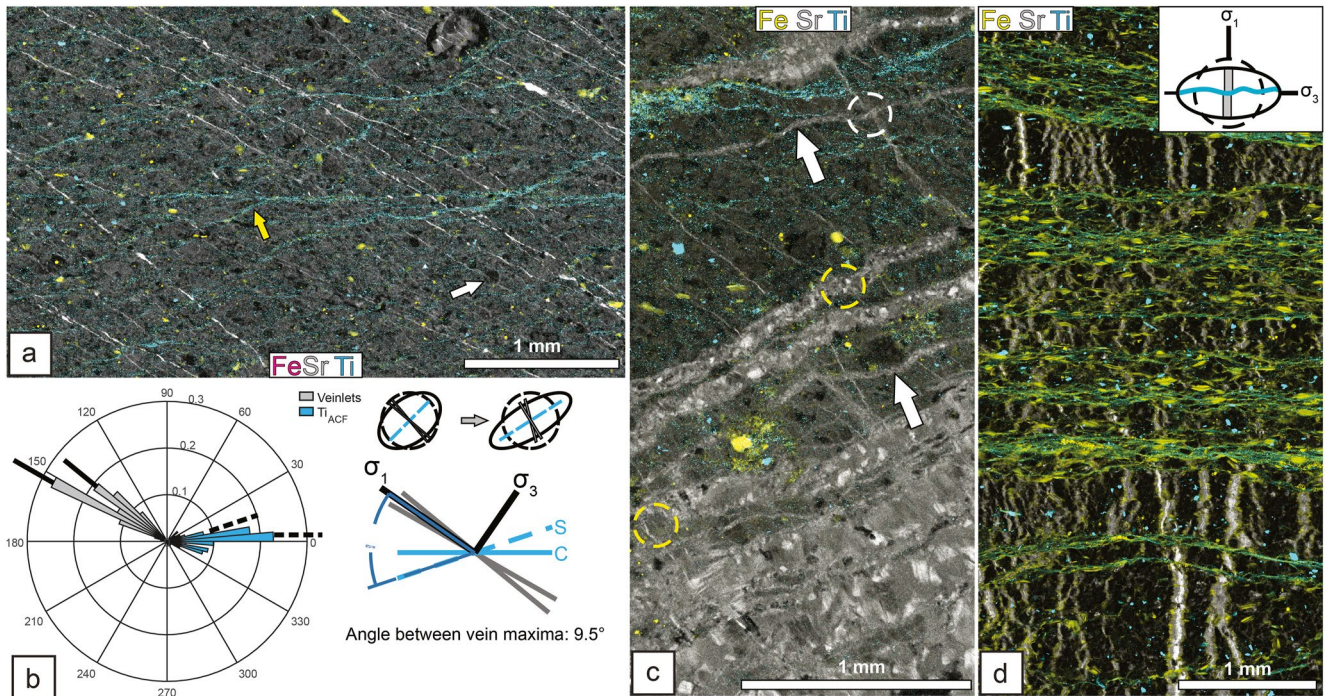


**Figure 11.** (a) Three-element XFM map of sample E2. A set of possibly conjugate, right-dipping micron-veinlets is characterized by high Sr concentrations (white colors). Secondary micas enriched in Ti (cyan) form an incipient SC-like fabric. The yellow arrow marks an S-plane curving into a horizontal C-plane. If the micron-veinlets are conjugate, they must have propagated as mixed-mode fractures. However, a shear displacement is not discernible. The white arrow marks a micron-veinlet cutting a round *Globigerina* shell. Hence, the two sets of veinlets might have formed at different times. Alternatively, the shear displacement could be below the level of resolution or at a high angle to the imaging plane. Given that the dihedral angle between veinlet sets is  $<10^\circ$ , the shear displacement should be much smaller than the  $10\ \mu\text{m}$  of opening displacement and hence at the resolution limit. (b) Polar plot of the orientation distribution for the micron-veinlets and Ti-rich foliation planes (left side). Stress-strain interpretation (right side) including strain ellipses of the structures in (a). The black arrows indicate the orientation of applied principal stresses. If the micron-veinlets form a conjugate low-strain set, the orientations of the in-plane principal stresses ( $\sigma_1$  and  $\sigma_3$ ) can be derived from the bisectors of their dihedral angle. The top sketch displays the classic simple-shear interpretation (Hancock, 1985) for the micron-veinlets (gray rectangles) and the S-plane (dashed blue line). Progressive general shear would lead to dextral rotation of both structures toward the shear plane. (c) Three-element map of the same sample shown in (a) with a set of parallel micron-veinlets cut by the steep micron-veinlets (dashed yellow circles). Rare older steep micron-veinlets are cut by the parallel veinlets (dashed white circle). This observation demonstrates that the parallel veinlets are preserved in their original emplacement orientation, as supported by the fact that the SC-like fabric is only incipient and thus of low finite strain (Akker et al., 2021a). (d) Three-element SFXM map of sample E1.1. Horizontal quartz-rich microlithons (mostly black) alternate with chlorite-rich foliation domains (enriched in Fe and Ti, see also Figure 8a). This foliation is cut orthogonally by calcite micron-veinlets, which are more strongly deformed or completely dissolved in the foliation domains. In microlithons, veinlets exhibit folding, dextral and sinistral rotation, and horizontal shearing along discrete, foliation-parallel shear bands. A pure-shear-like state of finite strain can explain these observations (see inset): the foliation forms normal to the incremental minimum principal strain and the veinlets parallel to it. Accordingly,  $\sigma_1$  is expected to be sub-perpendicular to the foliation.

the foliation and veins formed on the prograde metamorphic path until peak metamorphism was reached during accretion and thrusting of the studied paleo-wedge. Moreover, previous work from Ebert et al. (2007), Lahfid et al. (2010), and Rahn et al. (1995) determined that the samples studied here experienced peak metamorphic temperatures from 250 to 330°C (Figure 1). These temperatures are consistent with the observed penetrative dissolution-precipitation creep of phyllosilicates, quartz, and calcite forming the slate matrix of our samples (Figures 9a–9c; see also Akker et al., 2021a, 2021b). The associated penetrative foliation is only observed in samples with metamorphic peak temperatures  $>250^\circ\text{C}$  (Akker, 2020; Akker et al., 2021a; Dielforder et al., 2016). Therefore, the studied vein-arrays and the slate foliation must have formed in-situ, in the deeper parts of the inner wedge where temperature exceeded  $250^\circ\text{C}$ . Reliable depth estimates are difficult to obtain. For the Flysch of the Carpathian accretionary wedge of the Alpine orogenic system, geothermal gradients of in the range of  $17\text{--}29^\circ\text{C}/\text{km}$  with a mean of  $22^\circ\text{C}/\text{km}$  were estimated (Hurai et al., 2006). Dielforder et al. (2016) calculated a mean geothermal gradient of  $17^\circ\text{C}/\text{km}$  with a range of  $15\text{--}20^\circ\text{C}/\text{km}$  for the studied paleo-wedge under prograde conditions. Using these values, a maximum burial depth of ca. 22 km is obtained for peak-metamorphic conditions of our samples.

### 5.3. Vein Generations and State of Stress

Mutual overprint of deformation structures is typically interpreted as an indication for their formation during a large progressive deformation. At the timescale of such large deformation, the structures are then considered “coeval.” However, this does not necessarily mean that all structures generated during a progressive deformation event truly formed at the same time (synchronous formation). In our case, we observe clear evidence that steep and parallel veins alternate in their formation (diachronous formation). First, in all studied samples, there are clear one-way cross-cutting relationships between geometrically consistent sets of steep and parallel veins. Consider Figure 7 as an example. In the uppermost part of the image, a set of gently left-dipping, sheared steep veins with thicknesses of order tens to hundreds of microns (oldest set) is truncated by the largest parallel vein (second oldest set), which in turn is cut by steep micron-veinlets preserved in its interior (youngest set). Second, the Sr concentrations of cross-cutting vein set, always differ significantly, which can be explained by different fluid sources or differences in physico-chemical conditions during vein cementation (Cerchiari et al., 2020; Muñoz-Montecinos et al., 2020; Raimbourg et al., 2015; Vannucchi et al., 2010). Third, our micrographs show progressive vein overprint by the slate foliation accommodated by pressure-dissolution creep (e.g., Figures 9e and 9f). This is a fundamentally different deformation mechanism than brittle fracturing and operates at slower strain rates (Gratier et al., 1999, 2013). In concert, these observations imply that steep and parallel vein sets form repeatedly during distinct deformation episodes within a long-term progressive deformation event.

Since parallel and steep veinlets form in different orientations relative to the foliation, the question arises if they formed in the same far-field stress field or whether they developed because of transient stress flips, as suggested for G2/G3 veins by Dielforder et al. (2015), caused by megathrust earthquakes (Hu & Wang, 2006). Let us consider steep veins first. At the outcrop scale, we commonly observe pygmalically folded steep veins (Figures 3b and 3e). Both the emplacement of these veins and subsequent folding and rotation are consistent with a maximum principal stress at high angles to foliation. This picture is also observed repeatedly on the microscale: (a) we document veinlets emplaced progressively at high angles to the foliation subject to subsequent shearing and boudinage (Figure 9e). (b) Potentially conjugate steep veinlets whose bisector makes a ca. 45° angle with the C-planes of an incipient SC-like fabric in the slate foliation (Figures 6, 11a, and 11b) can also be explained with a maximum compression at high angle to the foliation. (c) We observe nearly perpendicular slate foliations and veinlets (Figures 8a and 9f), where the veinlets appear slightly folded, rotate dextrally and sinistrally, and are commonly sheared parallel to the foliation along phyllosilicates. This geometric relationship again indicates that the maximum principal stress was nearly normal to the foliation (see Figure 11d). In summary, the studied cogenetic (but diachronous) sets of steep veins and slate foliations show geometries indicative of progressive, generally non-coaxial deformation with a maximum principal stress at a steep angle to foliation between 45° and 90°, which in turn is consistent with a gently to moderately north-plunging (toward the foreland) maximum principal stress in the thrust regime, as expected for a subduction wedge under compression (Dielforder et al., 2015, 2016; Wang & Hu, 2006).

Our micrographs display a large spread of angles between steep veins and the foliation, ranging from as low as 30° (Figure 4) to 90° (Figures 4, 6, 9, and 11). This spread does not necessarily reflect time changes of the applied stress field but is best explained by the combined effects of large, progressive, localized deformation and geometric factors. We provide many clear examples of progressive general-shear deformation of steep and parallel veins at the outcrop scale (Figure 2) and microscale (Figures 4, 6–9, and 11). At the large scale, the thickening of the studied accretionary wedge is accommodated by regional folding and thrusting. Local differences in strain state (pure- vs. simple-shear-like) are controlled by the mechanical properties of the folded protolith beds and their position within larger folds, the limbs of which progressively rotated relative to the far-field stress field (Figure 12). Moreover, foliation orientation (via folding of bedding as well as fanning and refraction of secondary axial planar cleavage) and vein orientation vary systematically from hinge to limb, and layer to layer, in folds and as function of layer rheology and finite strain (Figure 12; Cosgrove, 1989; Liu et al., 2016; Schmalholz & Mancktelow, 2016). These points are very important when interpreting vein and foliation orientations in terms of paleo-stress and comparing them to the models in the literature (Dielforder et al., 2015, 2016; Wang & Hu, 2006), which assume small-strain deformation of a homogeneous 2D plane-strain, linear elastic wedge with perfect wedge geometry and flat plate interface. The structural inventory described here clearly deformed during very large, progressive, general shear involving significant internal volume change and highly heterogeneous 3D deformation of anisotropic rocks with complex visco-elasto-plastic rheology that changed over time and in space. Because of non-coaxial, large strain alone, most of the observed structures, foliations and veins alike, are most



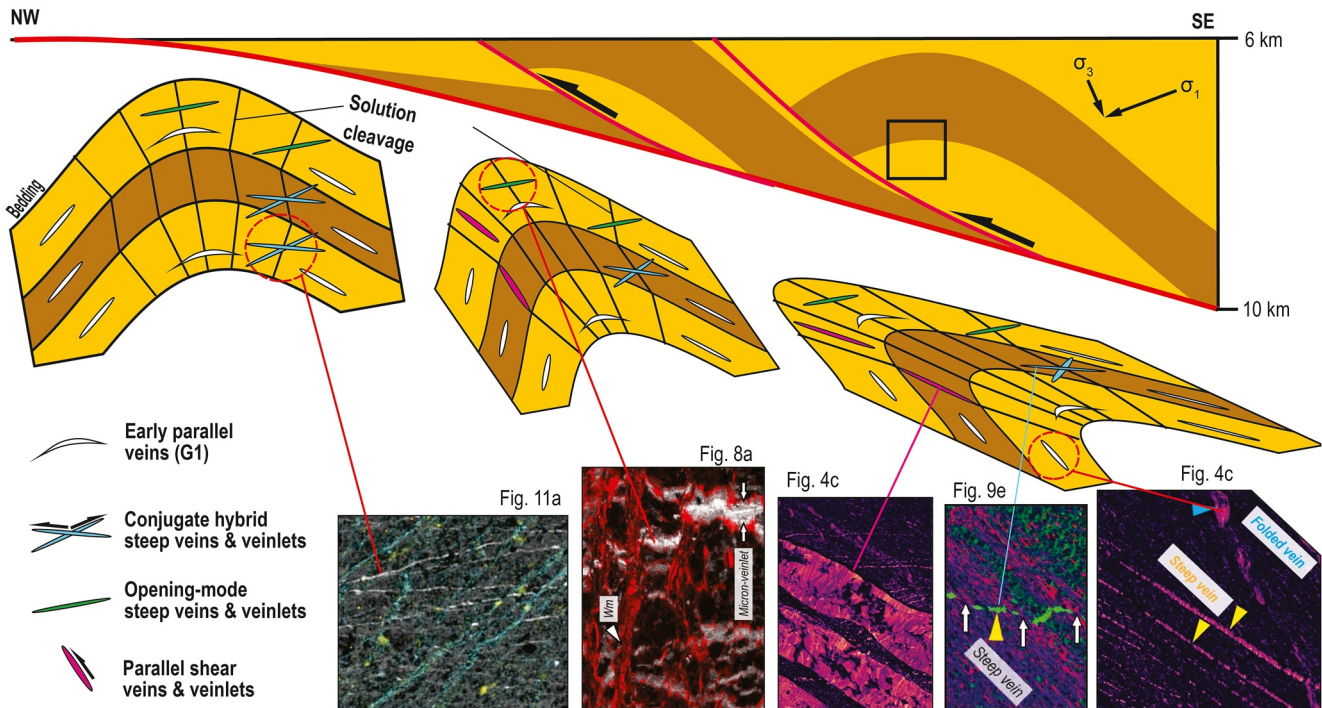


**Figure 12.** Link between the observed vein orientations relative to the foliation in the micrographs and the location within the large-scale folds in the accretionary wedge. The foliation orientation changes due to folding of the bedding as well as fanning and refraction of secondary axial planar cleavage. The vein orientations vary systematically from hinge to limb, and layer to layer, in folds and as function of layer rheology and finite strain in the accretionary wedge.

likely not preserved in the orientation in which they nucleated. Hence, it is not surprising that vein orientations are variable and do not conform with idealized stress directions modeled in the literature (notice the large spread of foliation and vein orientations in Figure 2b).

With this caveat in mind, let us consider the parallel veins next. One should assess if parallel veins are preserved in their emplacement orientation, considering the abundant evidence for non-coaxial deformation and associated rotation of steep veins toward the foliation plane. The low-strain sample shown in Figure 11c demonstrates that the parallel veinlets within it retain their original emplacement orientation and are not a result of transposition into the foliation due to large general shear (Figure 11c, see figure caption for explanation). Moreover, even in high-strain samples, one can generally argue that laterally continuous parallel veins are preserved close to their emplacement orientation. Steep veinlets subject to progressive general shear form disconnected boudins at moderate shear strains (Figures 7 and 9e) and transform into rootless isoclinal folds at high strain (Figure 9f). Therefore, it is reasonable to assume that parallel veins with well-preserved blocky texture and minor thickness changes due to pinch-and-swell structures were emplaced subparallel to the foliation.

Did the parallel veins form under the same stress state as the steep ones? Fagereng et al. (2010) demonstrated that foliation-parallel shear veins and high-angle (steep) extension veins can form coevally under a constant far-field maximum principal stress at high angles to foliation because of the mechanical weakness of the solution cleavage. In our research area, we do not observe textural indicators such as slickenfibers for foliation-parallel shear in outcrop-scale parallel veins. However, this can be the result of exposure bias. We observed most veins in creek beds, on surfaces highly polished by water, which possibly removed slickenfibers. Moreover, stepped parallel veins can be observed, in mutual overprint with ptgymatically folded, progressively sheared steep veins (Figure 3e). Both structures provide clear evidence for shear parallel to the foliation. In addition, many of our parallel veins are often quite thin (mm-range) with high aspect ratios (>50:1, Figures 3a, 3b, 3d, and 4a). These observations are in favor for a formation under non-coaxial conditions. Therefore, at least some layer-parallel veins represent shear veins with an opening component (i.e., extension plus shear, see vein sketches in Figure 10a; Bons et al., 2012), which could have formed under a maximum principal stress at high angles to foliation (Fagereng et al., 2010) in the thrusting regime.

However, Dielforder et al. (2015) documented foliation-parallel shear veins with top-to-S shear sense (G2) that formed in the inner wedge. This vein orientation and hanging-wall-down shear sense indicate a normal-faulting stress regime with a steeply north-plunging maximum principal stress, which the authors explained with a transient stress flip due to megathrust earthquakes. Since we cannot ascertain the shear sense for foliation-parallel shear veins in our study, we cannot determine if they formed in a thrusting- or normal-faulting regime. Both solutions are mechanically possible and have been observed in the field (Dielforder et al., 2015; Fagereng et al., 2010), and indeed one would expect to observe both types in a subduction wedge that experiences periods of stable and critical compression interrupted by seismically induced extensional periods. Dielforder et al. (2015) also documented steeply north-dipping, pure opening-mode veins formed in the inner wedge (G3) with angles of generally  $\leq 45^\circ$  to the south-dipping cleavage, also consistent with a normal-faulting regime. However, most of the steep micron-veinlets documented here (Figures 5 and 7–9) have angles  $> 80^\circ$  to the slaty cleavage, which is better explained with a thrust-fault stress regime, as discussed above.

#### 5.4. Toward a Conceptual Structural Model From Aseismic Outer Wedge to Inner Wedge Slow Slip and Megathrust Cycles

In the case of accretionary wedges, such as for example, in the Hikurangi subduction zone, slow slip events detected by GNSS data are very prominent features (Wallace, 2020; Wallace & Beavan, 2010; Wallace et al., 2012; Williams et al., 2013). Given the structural suite observed in the case of the paleowedge of the North Helvetic Flysch, our studied parallel shear veins might potentially be related to such slow slip events because they appear in large m-scale clusters with length on the order of tens of meters, possibly providing enough displacement for measurable seismicity. We therefore postulate that aforementioned cycles of layer-parallel veining and micro-veinlet formation could be related to slow slip events, in cases where the layer-parallel veins result from shear vein opening. On the contrary, inter-slip deformation was accommodated by viscous matrix deformation processes as documented in Akker et al. (2021a, 2021b, see also below). In this context, also the formation of micron-veinlets can be placed, where foliation-parallel stretching was accommodated by microcracking and mineral precipitation (Figure 10c). Note that these vein geometries and their kinematic framework are in good agreement with the common stress field in the inner wedge, generally characterized by a sub-horizontal maximum principal stress direction (see Figure 10c).

In the studied Flysch Units, Dielforder et al. (2015, 2016) additionally found isolated steep layer-parallel G2 shear veins, induced by normal faulting, and foliation-oblique G3 extension veins, respectively. They both require a steeply and slightly to the foreland inclined sigma one direction, which deviates by  $90^\circ$  from aforementioned general inner wedge stress field. Hence a stress flip is required, which Dielforder et al. (2015, 2016) attribute to switches from aseismic to co-seismic deformation during megathrust earthquakes. Hence, integrating over the entire vein inventory of the investigated North Helvetic Flysch paleowedge allows to discriminate between (a) early aseismic outer wedge deformation (G1 shear veins) and (b) slow and fast inner wedge veining events the latter being attributed to (c) slow slip and (d) megathrust earthquake cycles (G2 and G3, Figure 10c).

#### 5.5. Geological Controls on the Formation, Location, and Preservation Potential of Vein-Arrays

Our map (Figure 2a) shows that vein-arrays are not distributed homogeneously in the studied Flysch. Vein-arrays typically appear in slate-rich host rocks (see Figure 3), which implies that the protolith lithology has an impact on vein formation. Most creep laws for pressure dissolution indicate that strain rate is inversely proportional to grain size cubed in the case of grain boundary diffusion (Gratier et al., 2013). Moreover, up to a temperature of ca.  $300^\circ\text{C}$ , calcite seems to be more mobile than quartz via pressure dissolution (Gratier et al., 2013 and references therein). Hence, slates derived from very fine-grained, carbonate-rich silt- and claystones as well as calc-mudstones and wackestones are expected to deform very efficiently by pressure-dissolution creep. Microstructural evidence suggests that the propagating tips of stylolites and dissolution seams might feature transient high-porosity regions with high pore-fluid pressures (Carrio-Schaffhauser et al., 1990). Moreover, dissolution foliation and stylolites are commonly associated with cogenetic veins at high angles (Gratier et al., 2013; Toussaint et al., 2018). In other words, rock packages subject to low permeability and enhanced rates of pressure dissolution creep can readily form hydraulic fractures, which probably explains why vein-arrays are concentrated in slates in our research area. Moreover, rheological effects might contribute to array formation. The remarkably dense spacing of steep and parallel micron-veinlets (Figures 3, 4, 6, and 7) suggests that the cemented calcite veins



are mechanically stronger than the slate matrix (Virgo et al., 2014). In this case, the veins act as stiff inclusions forming stress concentrations around them (Eshelby, 1957), which are relaxed by fracture of the weaker matrix rock. This interpretation is supported by the fact that sheared steep veins form ptygmatic folds while passing through the shortening field, and asymmetric boudins once they enter the stretching field of the non-coaxial strain field, typical structures forming in shortened and lengthened strong layers (Schmalholz & Mancktelow, 2016). Hence, the higher strength of the veins might explain why both steep and parallel veins form densely spaced arrays on all studied length scales.

At the outcrop scale, parallel veins are more common than steep ones. This observation is possibly explained by the differences in preservation potential of both vein orientation families. Vein-arrays are continuously recycled into the slate matrix through shearing-assisted pressure-dissolution processes. This recycling process can be seen readily in our XFM maps on the example of the small micron-veinlets, which demonstrate that the preservation potential of steep veinlets is particularly poor in the slate matrix (Figures 9e and 9f). Because of their  $S_m$ -normal orientation (Figures 6 and 7) and their small width (<100  $\mu\text{m}$ ), steep micron-veinlets are easily incorporated into the matrix due to folding, shearing, and boudinage (Figures 9e and 9f) as well as pressure-dissolution resulting in their disappearance when being slate-hosted. The preservation potential of steep micron-veinlets is highest within parallel veins, which shield older vein-internal structures from recycling into the matrix. This is also true for slate domains, which became integrated into domains of accumulated  $S_m$ -parallel veins. If micron-veinlets are not shielded in bigger calcite veins, they are rapidly overprinted and recrystallized (e.g., micron-veinlets in the slate matrix of Figures 9e and 9f and S domains in Figure 5c). However, the predominant occurrence of micron-veinlets in layer-parallel veins may also be the consequence of rupture arrest at the boundary from vein to slate matrix. The strong mechanical layering of the slates might therefore play a role in their vein dominated occurrence (Philipp et al., 2013). As a result, it is clear that the number of steep micron-veinlets currently preserved and observed in our samples only represent a snapshot in time. The total amount of steep veinlets formed in the slates must have been much larger.

### 5.6. Implications for Paleo Fluid Transport and Fluid Sources

The mutual but diachronous overprinting of both vein families and the slate foliation indicates a progressive cyclic brittle-viscous deformation. This coexistence of brittle and viscous deformation processes at low-grade conditions has been observed in many other fossil accretionary wedges (e.g., Fagereng et al., 2010; Meneghini et al., 2009; Palazzin et al., 2016) and is consistent with microphysical models and experiments for low-grade deformation that describe the cooperation of slip on phyllosilicates, pressure-solution and fracturing processes (den Hartog & Spiers, 2013, 2014; Fagereng & Den Hartog, 2017), also known as frictional-viscous flow.

At the micro-scale, the foliation seams consist of phyllosilicate-rich layers, or foliation domains, that are separated by quartz- and calcite-rich microlithons (Figures 4b and 4d). This foliation assemblage clearly forms by pressure-solution creep (Figures 9a–9c, see also Akker et al., 2021a), where dissolution occurs perpendicular to the foliation and precipitation and directed mineral growth along it (Figure 9c). Thus, fluid transport and mass flux are focused parallel to the foliation. The steep micron-veinlets show a layer-normal orientation and are pervasively distributed throughout the deforming slate matrix as well as within layer-parallel calcite veins. The dense micron-veinlet fracture network is capable of temporarily hosting a considerable fluid volume in the wedge. Importantly, their length is sufficient to breach the phyllosilicate-rich foliation planes. Hence, we propose that these micron-veinlets represent distributed dynamic fracture porosity that relaxed intermittently critical pore fluid pressures produced by the stable, slow pressure-dissolution creep of the wedge. Such veinlets would allow large fluid volumes to migrate upwards in the wedge along the pressure gradient. In contrast, the layer-parallel veins arrange in obvious characteristic meter-scale vein-arrays, which in turn cluster as decameter-scale vein-arrays (Figure 2). This arrangement suggests that fluids are progressively localized during the formation of parallel-vein-arrays. Consequently, there are temporal switches between enhanced fluxes parallel or perpendicular to the foliation and vein arrays. From a time-integrated perspective and considering the close spatial proximity of both systems, it is conceivable that they feed each other during the alternating changes and recycle fluids locally, but over geological time scales they contribute to dehydrating the wedge with progressive accretion.

The cyclic brittle-viscous deformation also has important implications for the location and geometry of vein-arrays. Steep veins clearly form intermittently, marking the occurrence of episodic hydrofracturing events, which are interpreted to release cyclic pore-fluid pressure increases that build up during the slow pressure-dissolution creep

of the slate (Beach, 1977; Ramsay, 1980). If this hypothesis is correct, one expects that the source fluids for the steep veins are largely derived from the slate itself. This prediction has been proposed on the base of Sr-isotopes for G2 and G3 veins by Dielforder et al. (2015, 2016, 2022). Parallel veins may also be promoted by hydraulic fracturing requiring high pore-fluid pressures for their formation. Owing to their shear-induced nature and potential triggering by seismicity or slow slip activity, fluids may in fact be pumped from the adjacent matrix into the shear-induced dilatant pull-apart domains (Sibson et al., 1975), which can be tested by Sr isotopes. In fact, Dielforder et al. (2022) analyzed  $^{87}\text{Sr}/^{86}\text{Sr}$  ratios of vein carbonates from different generations within the Infra Helvetic Flysch Units. These authors found that the strontium isotopic evolution of the pore waters changes from an initial seawater signature (G1) to a composition of the host rock (G2 and G3) with increasing metamorphic grade. Moreover, the bulk pore fluid evolution seems to be unaffected by the influx of external metamorphic fluids. This indicates that the fluids for all generations of veins, including both the steep and parallel veins, were derived from the slate rock itself. This is another argument for the local fluid and mass transport processes in the matrix by dissolution-precipitation creep. Currently, however, we have no Sr isotope data for our layer-parallel shear veins. Supposedly they would show host-rock related Sr isotopic compositions, which needs to be tested in the future.

### 5.7. Potential Link to Transient Deformation and Seismicity Observed in Active Accretionary Wedges

The question arises, can we link the observed paleo-structures to seismicity at active plate boundaries? In modern subduction zones, different types of seismicity are reported, from megathrust earthquakes with moment magnitudes around  $M_w = 8$  to  $M_w = 9$  (e.g., Fujiwara et al., 2011; Leonard et al., 2010) to slow slip events with equivalent moment magnitudes also going up to  $M_w = 8$  (e.g., Schwartz & Rokosky, 2007). Slow earthquakes are not directly linked to a thermal or metamorphic regime or depth but rather show correlations with the amount of free  $\text{H}_2\text{O}$  fluid that becomes available due to metamorphic dehydration reactions (Peacock, 2009; Saffer & Wallace, 2015). Slow slip events and related tremor are therefore reported throughout a large depth range from the velocity-strengthening (stable-sliding) regime at the updip edge of the seismogenic zone to the velocity-strengthening regime at the downdip edge of the seismogenic zone (Schwartz & Rokosky, 2007). Examples of shallow slow slip are observed at the Hikurangi (Douglas et al., 2005; Eijsink & Ikari, 2022; Wallace & Beavan, 2010; Wallace et al., 2012), Northern Japan (Ito et al., 2013), Costa Rica (Dixon et al., 2014) and Nankai (Araki et al., 2017) wedges.

The observed fracturing events in the paleo-accretionary wedge represent a sudden increase in local strain rate that could potentially be seismic events with low magnitudes. As presented above, we have clear indications that in the studied accretionary wedge, the observed deformation features are closely linked to the hydro-mechanical cycle. We now speculate on the role of the paleo-structures as nuclei for seismicity or slow slip activity. Under the assumption of shear failure and following the approach of Behr and Bürgmann (2021) and Kotowski and Behr (2019), we plot the calculated seismic moment for our observed layer-parallel veins and vein-arrays with a series of lengths using:  $M_0 = \mu A d$ , where  $\mu$  is the shear modulus of the surrounding material,  $A$  is the source area, and  $d$  is the average slip. For the shear modulus, we take an average value reported for slates of 33 GPa (Wichert, 2020). The source area is calculated as:  $A = \pi r^2$ , where  $r$  is  $\frac{1}{2}$  of the entire fracture or vein length. The moment magnitude is then calculated using:  $M_w = (\log_{10}(M_0) - 16.1)/1.5$  (Kanamori, 1986). It is important to note that Kanamori's empirical scaling relationship requires that the seismic moment is expressed in dyn cm ( $1 \text{ dyn cm} = 10^{-7} \text{ Nm}$ ).

In order to create a megathrust earthquake with magnitude 8 or 9, a significant source area and meter-scale displacement are needed (Fujiwara et al., 2011; Leonard et al., 2010). Although the plate interface integrated over the entire front of the Alpine wedge may have hosted such megathrust events, our observed parallel-veins and vein-arrays with lengths up to 100 m, simply do not fall in that range.

If related to seismicity, our observed structures must therefore indicate smaller seismic events. Reported slow slip events from active plate boundaries show slip on the order of a few centimeters (Schwartz & Rokosky, 2007). However, since we do not have data on shear displacement for our observed structures, we simply assume that the lower-bound shear displacement is similar to the opening width of the layer-parallel veins (on average in the mm range). For an upper-bound estimate of shear displacement along the layer-parallel shear veins, we assume the m-scale, between 1 and 5 m (Figure 13). Note that this upper-bound displacement for a 100-m long shear vein corresponds to about 25% of that expected for a typical fault with the same length (Lathrop et al., 2022).



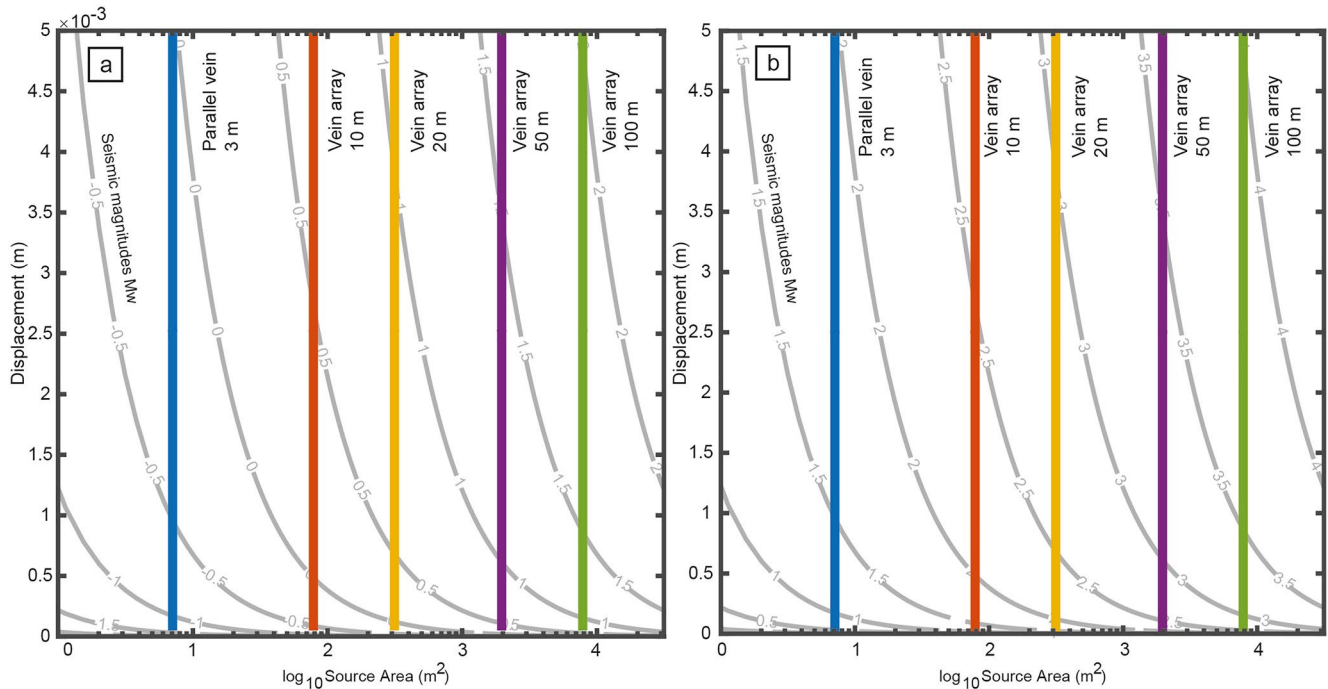


**Figure 13.** Seismic magnitude calculations for a series of parallel veins and vein-arrays with different length scales, following the approach of Behr and Bürgmann (2021) and Kotowski and Behr (2019). (a) Seismic magnitude calculations ( $M_w$ ) for layer-parallel veins where we assume the opening width represents the displacement and is on the  $\mu\text{m}$  to  $\text{cm}$ -range. These constraints are minimum estimates for  $M_w$ . (b) Seismic magnitude calculations ( $M_w$ ) for layer-parallel shear veins, where displacements are assumed to be at the  $\text{m}$ -scale. These constraints represents maximum estimates for  $M_w$ .

Our results show a range of magnitudes starting from  $M_w = 0.0$  for a layer-parallel vein with a length of 3 m and a displacement of 5 mm to  $M_w = 4.0$  for a vein-array with length of 100 m and a displacement of 4.5 m (Figures 13a and 13b). These lower and upper bound considerations give us a possible indication of what kind of magnitude we could expect for the observed layer-parallel veins. In the case of micro-veinlets, apertures in the range of 35  $\mu\text{m}$  and length scales of 2 cm would indicate very low  $M_w = -4.4$ , which are not detectable in current seismically active wedges with surface-based geophones. A major uncertainty exists on the absolute timing of veining events. We do not know if several layer-parallel veins or sets of micron-veinlets form simultaneously and, if so, over which distances they belong to a single rupture event. With enhanced lateral dimensions of such instantaneous fracture (vein) swarms, the associated potential seismic energy release would increase as well, resulting in higher magnitudes.

Our observations show similarities with the deeper part of the subduction zone, below the locked megathrust zone. In this part of the subduction zone, rheological heterogeneities, such as eclogites and coarse-grained blueschists, deform by brittle fracturing within a larger viscously deforming matrix. Such cyclic brittle ductile deformation (Giuntoli & Viola, 2022) and failure by fracturing of the rheological stiff patches could be ascribed to episodic tremor and slow slip (Behr & Bürgmann, 2021; Kotowski & Behr, 2019). In the studied accretionary wedge within the shallow part of the subduction zone, we also report a strong interaction of brittle and ductile deformation processes. Where veins act as stiff layers and inclusions within a ductile deforming slate matrix. As suggested by Behr and Bürgmann (2021) we also infer that despite the large thermal and chemical differences, the deformation structures and thus inferred rheological behavior in the accretionary wedge and the deep subduction interface are somewhat similar.

In summary, provided that the studied parts of the exhumed paleo-wedge were seismically active, the structures described above are the only ones we found that could be related to seismicity or slow slip activity. Alternatively, to fracturing and vein formation at seismic rates, hydro-fracturing could have occurred at non-seismic rates. Since the fracture and vein infilling processes as well their rates are related to each other, the vein infills in form of precipitation rates and amounts can give additional insights. In the case of quartz veins, Williams and Fagereng (2022) argue that the amount of precipitates and growth kinetics is problematic to be explained by earthquake and their recurrence time intervals, favoring diffusive flux in low flow regimes. Ujiie et al. (2018)

argues for fluids and fracturing induced by slow slip events, that is, at fast but non seismic rates. In the case of hydrothermal quartz vein systems and trace element concentrations, Berger and Herwegh (2019) and Raimbourg et al. (2021) show field vein examples which evolved under seismic conditions, with thin precipitates only after a single seismic event. Given all these constraints, in terms of vein precipitate volume and associated mass balances only the 10  $\mu\text{m}$  thick micron-veinlets or individual growth zones in layer-parallel veins could potentially be related to fast precipitation out of an advective fluid, which would be induced by fast isenthalpic pressure drop as is the case during seismic rupturing (e.g., Berger & Herwegh, 2019 and references therein). In contrast, the much thicker layer parallel-veins with their blocky texture and associated growth zonation patterns indicate calcite precipitation and idiomorphic growth of calcite crystals into an open pore space. We therefore infer, a main rapid fracturing event, generating a fracture with wide aperture, where calcite crystals continuously grow. Whether this growth was continuous or periodic cannot be treated here conclusively.

In sum, more work needs to be done to be more conclusive on the link between the subduction megathrust, the accretionary wedge and associated seismic activity. This requires future investigations on active as well as paleo-wedges and the exhumed plate interface.

## 6. Conclusion

We documented the geometry and spatial distribution of two different vein sets in the Flysch Units making up the late-stage accretionary wedge of the Alpine orogen. These two vein-sets mutually overprint each other as well as the ductile phyllosilicate-rich matrix. The latter accommodates deformation predominantly by pressure solution.

Our observations suggest:

- (1) The cyclic interaction between fracturing, veining and pressure solution is characteristic for the sediments in the inner part of the accretionary wedge at temperatures  $>250^{\circ}\text{C}$ .
- (2) With the use of XFM, we document pervasive veining on the micrometer-scale. Such micron-veinlets are not only present within competent bodies but are also pervasively distributed throughout the phyllosilicate-rich matrix.
- (3) The pervasive micron-veinlets enable episodic but diffuse foliation-perpendicular fluid migration through the wedge, linked to pressure solution in the phyllosilicate-rich matrix. This slow and continuous matrix deformation is likely active during aseismic stable wedge shortening.
- (4) The layer-parallel veins (meter-scale) with their arrangement in vein-arrays indicate a far more localized fluid transport. Their formation requires locally elevated pore fluid pressures and hydraulic failure probably owing to stress concentrations around pre-existing veins. If formed by seismic events, shear veins could potentially yield seismic activity in magnitudes of up to  $M_w = 4.0$ .
- (5) Cyclical stages of enhanced layer-parallel fluid flux alternate with those of layer perpendicular flow, allowing a short-intermediate term recycling of fluids between the two systems and on a long-term the progressive upward migration of fluids and therefore a dehydration of the wedge with progressive accretion and metamorphism.
- (6) Vein populations may record two hydromechanical cycles in the paleowedge with different time scales: In addition to (a) megathrust-earthquake induced stress flips with long reoccurrence times, (b) the cyclic formation of layer-parallel and steep micron-veinlets could indicate slow slip cycles in the wedge under low differential stress and high pore fluid pressures but much shorter reoccurrence intervals.
- (7) The frequent pervasive micro-scale brittle fracturing detected with XFM might not only be a local phenomenon but could be widespread throughout phyllosilicate-rich rocks in other exhumed accretionary wedges. Considering the very high spatial density, micron-veinlets must contribute significantly to the fluid budget of accretionary wedges.

## Conflict of Interest

The authors declare no conflicts of interest relevant to this study.

## Data Availability Statement

All data used in this manuscript will be made available in the Bern Open Repository and Information System (BORIS) and can also be found back in the PhD thesis from Dr. Ismay Vénice Akker: <https://doi.org/10.7892/boris.146962>.



### Acknowledgments

This work was supported by the Swiss National Science Foundation (SNSF, Grant 162340). Synchrotron X-ray fluorescence microscopy was undertaken on the X-ray fluorescence microscopy beamline at the Australian Synchrotron, part of ANSTO. CES acknowledges funding by the Australian Research Council through Grant DP170104550. We thank D. Fisher and two anonymous reviewers for their constructive reviews, that greatly helped improve the manuscript.

### References

- Akker, I. V. (2020). The evolution of slate microstructures during the accretion of foreland basin sediments and implications for mechanical strength, fluid flow and seismicity in accretionary wedges (Unpublished). Dissertation. Institute of Geological Sciences, Faculty of Science. <https://doi.org/10.7892/boris.146962>
- Akker, I. V., Berger, A., Schrank, C. E., Jones, M. W., Kewish, C. M., Klaver, J., & Herwegh, M. (2021a). The evolution of slate microfabrics during progressive accretion of foreland basin sediments. *Journal of Structural Geology*, *150*, 104404. <https://doi.org/10.1016/j.jsg.2021.104404>
- Akker, I. V., Berger, A., Zwingmann, H., Todd, A., Schrank, C. E., Jones, M. W., et al. (2021b). Structural and chemical resetting processes in white mica and their effect on K-Ar data during low temperature metamorphism. *Tectonophysics*, *800*, 228708. <https://doi.org/10.1016/j.tecto.2020.228708>
- Akker, I. V., Kaufmann, J., Desbois, G., Klaver, J., Urai, L. J., Berger, A., & Herwegh, M. (2018). Multiscale porosity changes along the pro-and retrograde deformation path: An example from Alpine slates. *Solid Earth*, *9*(5), 1141–1156. <https://doi.org/10.5194/se-9-1141-2018>
- Allmendinger, R. W., Cardozo, N., & Fisher, D. M. (2011). *Structural geology algorithms: Vectors and tensors*. Cambridge University Press.
- Araki, E., Saffer, D. M., Kopf, A. J., Wallace, L. M., Kimura, T., Machida, Y., et al. (2017). Recurring and triggered slow-slip events near the trench at the Nankai Trough subduction megathrust. *Science*, *356*(6343), 1157–1160. <https://doi.org/10.1126/science.aan3120>
- Bachmann, R., Oncken, O., Glodny, J., Seifert, W., Georgieva, V., & Sudo, M. (2009). Exposed plate interface in the European Alps reveals fabric styles and gradients related to an ancient seismogenic coupling zone. *Journal of Geophysical Research*, *114*(B5), B05402. <https://doi.org/10.1029/2008jb005927>
- Badertscher, N. P., Beaudoin, G., Therrien, R., & Burkhard, M. (2002). Glarus overthrust: A major pathway for the escape of fluids out of the Alpine orogen. *Geology*, *30*(10), 875–878. [https://doi.org/10.1130/0091-7613\(2002\)030<0875:goampf>2.0.co;2](https://doi.org/10.1130/0091-7613(2002)030<0875:goampf>2.0.co;2)
- Badertscher, N. P., & Burkhard, M. (2000). Brittle-ductile deformation in the Glarus thrust Lochseiten (LK) calc-mylonite. *Terra Nova*, *12*(6), 281–288. <https://doi.org/10.1046/j.1365-3121.2000.00310.x>
- Beach, A. (1977). Vein arrays, hydraulic fractures and pressure-solution structures in a deformed flysch sequence S.W. England. *Tectonophysics*, *40*(3), 201–225. [https://doi.org/10.1016/0040-1951\(77\)90066-x](https://doi.org/10.1016/0040-1951(77)90066-x)
- Behr, W. M., & Bürgmann, R. (2021). What's down there? The structures, materials and environment of deep-seated slow slip and tremor. *Philosophical Transactions of the Royal Society A: Mathematical, Physical & Engineering Sciences*, *379*(2193), 20200218. <https://doi.org/10.1098/rsta.2020.0218>
- Behrmann, J. H. (1991). Conditions for hydrofracture and the fluid permeability of accretionary wedges. *Earth and Planetary Science Letters*, *107*(3–4), 550–558. [https://doi.org/10.1016/0012-821x\(91\)90100-v](https://doi.org/10.1016/0012-821x(91)90100-v)
- Berger, A., & Herwegh, M. (2019). Cockade structures as a paleo-earthquake proxy in upper crustal hydrothermal systems. *Scientific Reports*, *9*(1), 9209. <https://doi.org/10.1038/s41598-019-45488-2>
- Bilek, S. L., & Lay, T. (1998). Variation of interplate fault zone properties with depth in the Japan subduction zone. *Science*, *281*(5380), 1175–1178. <https://doi.org/10.1126/science.281.5380.1175>
- Bons, P. D., Elburg, M. A., & Gomez-Rivas, E. (2012). A review of the formation of tectonic veins and their microstructures. *Journal of Structural Geology*, *43*(0), 33–62. <https://doi.org/10.1016/j.jsg.2012.07.005>
- Boulton, C., Mizera, M., Niemeijer, A. R., Little, T. A., Müller, I. A., Ziegler, M., & Hamers, M. F. (2022). Observational and theoretical evidence for frictional-viscous flow at shallow crustal levels. *Lithos*, *428*, 106831. <https://doi.org/10.1016/j.lithos.2022.106831>
- Byrne, D. E., Davis, D. M., & Sykes, L. R. (1988). Loci and maximum size of thrust earthquakes and the mechanics of the shallow region of subduction zones. *Tectonics*, *7*(4), 833–857. <https://doi.org/10.1029/tc007i004p00833>
- Cardozo, N., & Allmendinger, R. W. (2013). Spherical projections with OSXstereonet. *Computers & Geosciences*, *51*, 193–205. <https://doi.org/10.1016/j.cageo.2012.07.021>
- Carriero-Schaffhauser, E., Raynaud, S., Latière, H. J., & Mazerolle, F. (1990). Propagation and localization of stylolites in limestones. *Geological Society, London, Special Publications*, *54*(1), 193–199. <https://doi.org/10.1144/gsl.sp.1990.054.01.19>
- Cerchiari, A., Remitti, F., Mittempergher, S., Festa, A., Lugli, F., & Cipriani, A. (2020). Cyclical variations of fluid sources and stress state in a shallow megathrust-zone mélange. *Journal of the Geological Society*, *177*(3), 647–659. <https://doi.org/10.1144/jgs2019-072>
- Cosgrove, J. W. (1989). Cleavage, folding and the finite strain ellipsoid. *Proceedings—Geologists' Association*, *100*(4), 461–479. [https://doi.org/10.1016/s0016-7878\(89\)80022-7](https://doi.org/10.1016/s0016-7878(89)80022-7)
- Cox, S. F., Etheridge, M. A., & Wall, V. J. (1987). The role of fluids in syntectonic mass transport, and the localization of metamorphic vein-type ore deposits. *Ore Geology Reviews*, *2*(1–3), 65–86. [https://doi.org/10.1016/0169-1368\(87\)90024-2](https://doi.org/10.1016/0169-1368(87)90024-2)
- Dahlen, F. (1984). Noncohesive critical Coulomb wedges: An exact solution. *Journal of Geophysical Research*, *89*(B12), 10125–10133. <https://doi.org/10.1029/jb089ib12p10125>
- Dahlen, F. (1990). Critical taper model of fold-and-thrust belts and accretionary wedges. *Annual Review of Earth and Planetary Sciences*, *18*(1), 55–99. <https://doi.org/10.1146/annurev.ea.18.050190.000415>
- Davis, D., Suppe, J., & Dahlen, F. (1983). Mechanics of fold-and-thrust belts and accretionary wedges. *Journal of Geophysical Research*, *88*(B2), 1153–1172. <https://doi.org/10.1029/jb088ib02p01153>
- den Brok, R. C. O. K. (2021). Blatt 1174 Elm-Geologischer Atlas der Schweiz 1:25000 Karte 173.
- den Hartog, S. A., & Spiers, C. J. (2013). Influence of subduction zone conditions and gouge composition on frictional slip stability of megathrust faults. *Tectonophysics*, *600*, 75–90. <https://doi.org/10.1016/j.tecto.2012.11.006>
- den Hartog, S. A., & Spiers, C. J. (2014). A microphysical model for fault gouge friction applied to subduction megathrusts. *Journal of Geophysical Research: Solid Earth*, *119*(2), 1510–1529. <https://doi.org/10.1002/2013jb010580>
- Dewey, J. F., & Bird, J. M. (1970). Mountain belts and the new global tectonics. *Journal of Geophysical Research*, *75*(14), 2625–2647. <https://doi.org/10.1029/jb075i014p02625>
- Dielforder, A., Berger, A., & Herwegh, M. (2016). The accretion of foreland basin sediments during early stages of continental collision in the European Alps and similarities to accretionary wedge tectonics. *Tectonics*, *35*(10), 2216–2238. <https://doi.org/10.1002/2015tc004101>
- Dielforder, A., Villa, I. M., Berger, A., & Herwegh, M. (2022). Tracing wedge-internal deformation by means of strontium isotope systematics of vein carbonates. *Geological Magazine*, *159*(11–12), 1–15. <https://doi.org/10.1017/s0016756821001357>
- Dielforder, A., Vollstaedt, H., Vennemann, T., Berger, A., & Herwegh, M. (2015). Linking megathrust earthquakes to brittle deformation in a fossil accretionary complex. *Nature Communications*, *6*(1), 7504. <https://doi.org/10.1038/ncomms8504>
- Dixon, T. H., Jiang, Y., Malservisi, R., McCaffrey, R., Voss, N., Protti, M., & Gonzalez, V. (2014). Earthquake and tsunami forecasts: Relation of slow slip events to subsequent earthquake rupture. *Proceedings of the National Academy of Sciences of the United States of America*, *111*(48), 17039–17044. <https://doi.org/10.1073/pnas.1412299111>

- Douglas, A., Beavan, J., Wallace, L., & Townend, J. (2005). Slow slip on the northern Hikurangi subduction interface, New Zealand. *Geophysical Research Letters*, 32(16), L16305. <https://doi.org/10.1029/2005gl023607>
- Ebert, A., Herwegh, M., & Pfiffner, A. (2007). Cooling induced strain localization in carbonate mylonites within a large-scale shear zone (Glarus thrust, Switzerland). *Journal of Structural Geology*, 29(7), 1164–1184. <https://doi.org/10.1016/j.jsg.2007.03.007>
- Eijssink, A., & Ikari, M. (2022). Plate-rate frictional behavior of sediment inputs to the Hikurangi subduction margin: How does lithology control slow slip events? *Geochemistry, Geophysics, Geosystems*, 23(6), e2022GC010369. <https://doi.org/10.1029/2022gc010369>
- Eshelby, J. D. (1957). The determination of the elastic field of an ellipsoidal inclusion, and related problems. *Proceedings of the Royal Society of London. Series A, Mathematical and Physical Sciences*, 241(1226), 376–396. <http://www.jstor.org/stable/100095>
- Fagereng, Å., & Den Hartog, S. A. (2017). Subduction megathrust creep governed by pressure solution and frictional–viscous flow. *Nature Geoscience*, 10(1), 51–57. <https://doi.org/10.1038/ngeo2857>
- Fagereng, Å., Remitti, F., & Sibson, R. H. (2010). Shear veins observed within anisotropic fabric at high angles to the maximum compressive stress. *Nature Geoscience*, 3(7), 482–485. <https://doi.org/10.1038/ngeo898>
- Fisher, D., & Byrne, T. (1987). Structural evolution of underthrust sediments, Kodiak Islands, Alaska. *Tectonics*, 6(6), 775–793. <https://doi.org/10.1029/tc006i006p00775>
- Fisher, D. M., & Brantley, S. L. (2014). The role of silica redistribution in the evolution of slip instabilities along subduction interfaces: Constraints from the Kodiak accretionary complex, Alaska. *Journal of Structural Geology*, 69, 395–414. <https://doi.org/10.1016/j.jsg.2014.03.010>
- Frisch, W. (1979). Tectonic progradation and plate tectonic evolution of the Alps. *Tectonophysics*, 60(3–4), 121–139. [https://doi.org/10.1016/0040-1951\(79\)90155-0](https://doi.org/10.1016/0040-1951(79)90155-0)
- Fujiwara, T., Kodaira, S., No, T., Kaiho, Y., Takahashi, N., & Kaneda, Y. (2011). The 2011 Tohoku-Oki earthquake: Displacement reaching the trench axis. *Science*, 334(6060), 1240. <https://doi.org/10.1126/science.1211554>
- Gasser, D., & Den Brok, B. (2008). Tectonic evolution of the Engi slates, Glarus alps, Switzerland. *Swiss Journal of Geosciences*, 101(2), 311–322. <https://doi.org/10.1007/s00015-008-1258-0>
- Giuntoli, F., & Viola, G. (2022). A likely geological record of deep tremor and slow slip events from a subducted continental broken formation. *Scientific Reports*, 12(1), 1–14. <https://doi.org/10.1038/s41598-022-08489-2>
- Gratier, J.-P., Dysthe, D. K., & Renard, F. (2013). Chapter 2—The role of pressure solution creep in the ductility of the Earth's upper crust. In R. Dmowska (Ed.), *Advances in geophysics* (Vol. 54, pp. 47–179). Elsevier.
- Gratier, J.-P., Renard, F., & Labaume, P. (1999). How pressure solution creep and fracturing processes interact in the upper crust to make it behave in both a brittle and viscous manner. *Journal of Structural Geology*, 21(8), 1189–1197. [https://doi.org/10.1016/s0191-8141\(99\)00035-8](https://doi.org/10.1016/s0191-8141(99)00035-8)
- Groshong, R. H., Jr., Pfiffner, O. A., & Pringle, L. R. (1984). Strain partitioning in the Helvetic thrust belt of eastern Switzerland from the leading edge to the internal zone. *Journal of Structural Geology*, 6(1–2), 5–18. [https://doi.org/10.1016/0191-8141\(84\)90079-8](https://doi.org/10.1016/0191-8141(84)90079-8)
- Hancock, P. L. (1985). Brittle microtectonics: Principles and practice. *Journal of Structural Geology*, 7(3–4), 437–457. [https://doi.org/10.1016/0191-8141\(85\)90048-3](https://doi.org/10.1016/0191-8141(85)90048-3)
- Handy, M. R., Schmid, S. M., Bousquet, R., Kissling, E., & Bernoulli, D. (2010). Reconciling plate-tectonic reconstructions of Alpine Tethys with the geological–geophysical record of spreading and subduction in the Alps. *Earth-Science Reviews*, 102(3–4), 121–158. <https://doi.org/10.1016/j.earscirev.2010.06.002>
- Heilbronner, R. (2002). Analysis of bulk fabrics and microstructure variations using tessellations of autocorrelation functions. *Computers & Geosciences*, 28(4), 447–455. [https://doi.org/10.1016/s0098-3004\(01\)00088-7](https://doi.org/10.1016/s0098-3004(01)00088-7)
- Heilbronner, R., & Barrett, S. (2014). Image analysis. In *Image analysis in Earth sciences* (p. 137156). Springer.
- Henke, B. L., Gullikson, E. M., & Davis, J. C. (1993). X-ray interactions: Photoabsorption, scattering, transmission, and reflection at E= 50–30,000 eV, Z= 1–92. *Atomic Data and Nuclear Data Tables*, 54(2), 181–342. <https://doi.org/10.1006/adnd.1993.1013>
- Herwegh, M., Berger, A., Glotzbach, C., Wangenheim, C., Mock, S., Wehrens, P., et al. (2020). Late stages of continent-continent collision: Timing, kinematic evolution, and exhumation of the Northern rim (Aar Massif) of the Alps. *Earth-Science Reviews*, 200, 102959. <https://doi.org/10.1016/j.earscirev.2019.102959>
- Herwegh, M., Hürzeler, J.-P., Pfiffner, O. A., Schmid, S. M., Abart, R., & Ebert, A. (2008). The Glarus thrust: Excursion guide and report of a field trip of the swiss tectonic studies Group (swiss Geological society, 14.–16. 09. 2006). *Swiss Journal of Geosciences*, 101(2), 323–340. <https://doi.org/10.1007/s00015-008-1259-z>
- Howard, D. L., de Jonge, M. D., Afshar, N., Ryan, C. G., Kirkham, R., Reinhardt, J., et al. (2020). The XFM beamline at the Australian Synchrotron. *Journal of Synchrotron Radiation*, 27(5), 1447–1458. <https://doi.org/10.1107/s1600577520010152>
- Hu, Y., & Wang, K. (2006). Bending-like behavior of thin wedge-shaped elastic fault blocks. *Journal of Geophysical Research*, 111(B6), B06409. <https://doi.org/10.1029/2005jb003987>
- Hurai, V., Marko, F., Tokarski, A. K., Świerczewska, A., Kotulová, J., & Biroň, A. (2006). Fluid inclusion evidence for deep burial of the Tertiary accretionary wedge of the Carpathians. *Terra Nova*, 18(6), 440–446. <https://doi.org/10.1111/j.1365-3121.2006.00710.x>
- Hürzeler, J.-P., & Abart, R. (2008). Fluid transport and rock alteration along the Glarus thrust. *Swiss Journal of Geosciences*, 101(2), 251–268. <https://doi.org/10.1007/s00015-008-1265-1>
- Hyndman, R. D., Yamano, M., & Oleskevich, D. A. (1997). The seismogenic zone of subduction thrust faults. *Island Arc*, 6(3), 244–260. <https://doi.org/10.1111/j.1440-1738.1997.tb00175.x>
- Ito, Y., Hino, R., Kido, M., Fujimoto, H., Osada, Y., Inazu, D., et al. (2013). Episodic slow slip events in the Japan subduction zone before the 2011 Tohoku-Oki earthquake. *Tectonophysics*, 600, 14–26. <https://doi.org/10.1016/j.tecto.2012.08.022>
- Kanamori, H. (1986). Rupture process of subduction-zone earthquakes. *Annual Review of Earth and Planetary Sciences*, 14(1), 293–322. <https://doi.org/10.1146/annurev.ea.14.050186.001453>
- Kastner, M., Elderfield, H., & Martin, J. (1991). Fluids in convergent margins: What do we know about their composition, origin, role in diagenesis and importance for oceanic chemical fluxes? *Philosophical Transactions of the Royal Society of London. Series A: Physical and Engineering Sciences*, 335(1638), 243–259.
- Kotowski, A. J., & Behr, W. M. (2019). Length scales and types of heterogeneities along the deep subduction interface: Insights from exhumed rocks on Syros Island, Greece. *Geosphere*, 15(4), 1038–1065. <https://doi.org/10.1130/ges02037.1>
- Lahfid, A., Beyssac, O., Deville, E., Negro, F., Chopin, C., & Goffé, B. (2010). Evolution of the Raman spectrum of carbonaceous material in low-grade metasediments of the Glarus Alps (Switzerland). *Terra Nova*, 22(5), 354–360. <https://doi.org/10.1111/j.1365-3121.2010.00956.x>
- Lathrop, B. A., Jackson, C., Bell, R. E., & Rotevatn, A. (2022). Displacement/length scaling relationships for normal faults: a review, critique, and revised compilation. *Frontiers in Earth Science*, 10, 907543. <https://doi.org/10.3389/feart.2022.907543>
- Leonard, L. J., Currie, C. A., Mazzotti, S., & Hyndman, R. D. (2010). Rupture area and displacement of past Cascadia great earthquakes from coastal coseismic subsidence. *Bulletin*, 122(11–12), 2079–2096. <https://doi.org/10.1130/b30108.1>
- Lihou (1995). *The early evolution and deformation of the North Alpine Foreland Basin, eastern Swiss Alps*. University of Oxford.



- Lihou (1996). Structure and deformational history of the Infracaralpetic flysch units, Glarus Alps, eastern Switzerland. *Eclogae Geologicae Helveticae*, 89(1), 439–460.
- Liu, X., Eckert, A., & Connolly, P. (2016). Stress evolution during 3D single-layer visco-elastic buckle folding: Implications for the initiation of fractures. *Tectonophysics*, 679, 140–155. <https://doi.org/10.1016/j.tecto.2016.04.042>
- Maltman, A., & Vannucchi, P. (2004). Insights from the Ocean Drilling Program on shear and fluid-flow at the mega-faults between actively converging plates. *Geological Society, London, Special Publications*, 224(1), 127–140. <https://doi.org/10.1144/gsl.sp.2004.224.01.09>
- Meneghini, F., Marroni, M., Moore, J., Pandolfi, L., & Rowe, C. (2009). The processes of underthrusting and underplating in the geologic record: Structural diversity between the Franciscan Complex (California), the Kodiak Complex (Alaska) and the Internal Ligurian Units (Italy). *Geological Journal*, 44(2), 126–152. <https://doi.org/10.1002/gj.1144>
- Meneghini, F., Marroni, M., & Pandolfi, L. (2007). Fluid transport during accretion in sediment-dominated margins: Evidence of a high-permeability fossil fault zone from the Internal Ligurian accretionary units of the Northern Apennines, Italy. *Journal of Structural Geology*, 29(3), 515–529. <https://doi.org/10.1016/j.jsg.2006.10.003>
- Meneghini, F., & Moore, J. C. (2007). Deformation and hydrofracture in a subduction thrust at seismogenic depths: The Rodeo Cove thrust zone, Marin Headlands, California. *Geological Society of America Bulletin*, 119(1–2), 174–183. <https://doi.org/10.1130/b25807.1>
- Milnes, A. G., & Pfiffner, O.-A. (1977). Structural development of the Infracaralpetic complex, eastern Switzerland. *Eclogae Geologicae Helveticae*, 70(1), 83–95.
- Mittepergher, S., Cerchiari, A., Remitti, F., & Festa, A. (2018). From soft sediment deformation to fluid assisted faulting in the shallow part of a subduction megathrust analogue: The Sestola Vidiciatico tectonic Unit (Northern Apennines, Italy). *Geological Magazine*, 155(2), 438–450. <https://doi.org/10.1017/s0016756817000668>
- Moore, J. C., & Saffer, D. (2001). Updip limit of the seismogenic zone beneath the accretionary prism of southwest Japan: An effect of diagenetic to low-grade metamorphic processes and increasing effective stress. *Geology*, 29(2), 183–186. [https://doi.org/10.1130/0091-7613\(2001\)029<0183:ulotz>2.0.co;2](https://doi.org/10.1130/0091-7613(2001)029<0183:ulotz>2.0.co;2)
- Moore, J. C., & Vrolijk, P. (1992). Fluids in accretionary prisms. *Reviews of Geophysics*, 30(2), 113–135. <https://doi.org/10.1029/92rg00201>
- Muñoz-Montecinos, J., Angiboust, S., Cambeses, A., & García-Casco, A. (2020). Multiple veining in a paleo-accretionary wedge: The metamorphic rock record of prograde dehydration and transient high pore-fluid pressures along the subduction interface (Western Series, central Chile). *Geosphere*, 16(3), 765–786. <https://doi.org/10.1130/ges02227.1>
- Musso Piantelli, F. M., Mair, D., Berger, A., Schlunegger, F., Wiederkehr, M., Kurmann, E., et al. (2022). 4D reconstruction of the Doldenhorn nappe-basement system in the Aar massif: Insights into late-stage continent-continent collision in the Swiss Alps. *Tectonophysics*, 843, 229586. <https://doi.org/10.1016/j.tecto.2022.229586>
- Nibourel, L., Berger, A., Egli, D., Heuberger, S., & Herwegh, M. (2021). Structural and thermal evolution of the eastern Aar Massif: Insights from structural field work and Raman thermometry. *Swiss Journal of Geosciences*, 114(1), 1–43. <https://doi.org/10.1186/s00015-020-00381-3>
- Palazzin, G., Raimbourg, H., Famin, V., Jolivet, L., Kusaba, Y., & Yamaguchi, A. (2016). Deformation processes at the down-dip limit of the seismogenic zone: The example of Shimanto accretionary complex. *Tectonophysics*, 687, 28–43. <https://doi.org/10.1016/j.tecto.2016.08.013>
- Peacock, S. M. (2009). Thermal and metamorphic environment of subduction zone episodic tremor and slip. *Journal of Geophysical Research*, 114(B8), B00A07. <https://doi.org/10.1029/2008jb005978>
- Pfiffner, O. A. (1977). *tektonische Untersuchungen im Infracaralpetikum der Ostschweiz*. ETH Zurich.
- Pfiffner, O. A. (1985). Displacements along thrust faults. *Eclogae Geologicae Helveticae*, 78(2), 313–333.
- Pfiffner, O. A. (1986). Evolution of the north Alpine foreland basin in the Central Alps. *Foreland basins*, 219–228. <https://doi.org/10.1002/9781444303810.ch11>
- Pfiffner, O. A. (1993). The structure of the Helvetic nappes and its relation to the mechanical stratigraphy. *Journal of Structural Geology*, 15(3–5), 511–521. [https://doi.org/10.1016/0191-8141\(93\)90145-z](https://doi.org/10.1016/0191-8141(93)90145-z)
- Pfiffner, O. A., Ramsay, J., & Schmid, S. (2011). Structural map of the Helvetic Zone of the Swiss Alps. *Geological Special Map*, 1(100,000).
- Philipp, S. L., Afşar, F., & Gudmundsson, A. (2013). Effects of mechanical layering on hydrofracture emplacement and fluid transport in reservoirs. *Frontiers in Earth Science*, 1, 4. <https://doi.org/10.3389/feart.2013.00004>
- Poulet, T., Veveakis, M., Herwegh, M., Buckingham, T., & Regenauer-Lieb, K. (2014). Modeling episodic fluid-release events in the ductile carbonates of the Glarus thrust. *Geophysical Research Letters*, 41(20), 7121–7128. <https://doi.org/10.1002/2014gl061715>
- Pytte, A., & Reynolds, R. (1989). The thermal transformation of smectite to illite. In *Thermal history of sedimentary basins* (pp. 133–140). Springer.
- Rahn, M., Mullis, J., Erdelbrock, K., & Frey, M. (1995). Alpine metamorphism in the north Helvetic flysch of the Glarus-Alps, Switzerland. *Eclogae Geologicae Helveticae*, 88(1), 157–178.
- Raimbourg, H., Augier, R., Famin, V., Gadenne, L., Palazzin, G., Yamaguchi, A., & Kimura, G. (2014). Long-term evolution of an accretionary prism: The case study of the Shimanto Belt, Kyushu, Japan. *Tectonics*, 33(6), 936–959. <https://doi.org/10.1002/2013tc003412>
- Raimbourg, H., Famin, V., Palazzin, G., Yamaguchi, A., Augier, R., Kitamura, Y., & Sakaguchi, A. (2019). Distributed deformation along the subduction plate interface: The role of tectonic mélanges. *Lithos*, 334, 69–87. <https://doi.org/10.1016/j.lithos.2019.01.033>
- Raimbourg, H., Rajič, K., Moris-Muttoni, B., Famin, V., Palazzin, G., Fisher, D., et al. (2021). Quartz vein geochemistry records deformation processes in convergent zones. *Geochemistry, Geophysics, Geosystems*, 22(4), e2020GC009201. <https://doi.org/10.1029/2020gc009201>
- Raimbourg, H., Vacelet, M., Ramboz, C., Famin, V., Augier, R., Palazzin, G., et al. (2015). Fluid circulation in the depths of accretionary prisms: An example of the Shimanto Belt, Kyushu, Japan. *Tectonophysics*, 655, 161–176. <https://doi.org/10.1016/j.tecto.2015.05.023>
- Ramsay, J. G. (1980). The crack–seal mechanism of rock deformation. *Nature*, 284(5752), 135–139. <https://doi.org/10.1038/284135a0>
- Ryan, C. G., Etschmann, B. E., Vogt, S., Maser, J., Harland, C. L., van Achterbergh, E., & Legnini, D. (2005). Nuclear microprobe—Synchrotron synergy: Towards integrated quantitative real-time elemental imaging using PIXE and SXRF. *Nuclear Instruments and Methods in Physics Research B*, 231(1–4), 183–188. <https://doi.org/10.1016/j.nimb.2005.01.054>
- Ryan, C. G., & Jamieson, D. N. (1993). Dynamic analysis: On-line quantitative PIXE microanalysis and its use in overlap-resolved elemental mapping. *Nuclear Instruments and Methods in Physics Research B*, 77(1–4), 203–214. [https://doi.org/10.1016/0168-583x\(93\)95545-g](https://doi.org/10.1016/0168-583x(93)95545-g)
- Saffer, D. M., & Tobin, H. J. (2011). Hydrogeology and mechanics of subduction zone forearcs: Fluid transport and pore pressure. *Annual Review of Earth and Planetary Sciences*, 39(1), 157–186. <https://doi.org/10.1146/annurev-earth-040610-133408>
- Saffer, D. M., & Wallace, L. M. (2015). The frictional, hydrologic, metamorphic and thermal habitat of shallow slow earthquakes. *Nature Geoscience*, 8(8), 594–600. <https://doi.org/10.1038/ngeo2490>
- Schmalholz, S. M., & Mancktelow, N. S. (2016). Folding and necking across the scales: A review of theoretical and experimental results and their applications. *Solid Earth*, 7(5), 1417–1465. <https://doi.org/10.5194/se-7-1417-2016>
- Schmid, S. M. (1975). The Glarus overthrust: Field evidence and mechanical model.

- Schmid, S. M., Fügenschuh, B., Kissling, E., & Schuster, R. (2004). Tectonic map and overall architecture of the Alpine orogen. *Eclogae Geologicae Helveticae*, 97(1), 93–117. <https://doi.org/10.1007/s00015-004-1113-x>
- Schmid, S. M., Kissling, E., Diehl, T., van Hinsbergen, D. J., & Molli, G. (2017). Ivrea mantle wedge, arc of the Western Alps, and kinematic evolution of the Alps–Apennines orogenic system. *Swiss Journal of Geosciences*, 110(2), 581–612. <https://doi.org/10.1007/s00015-016-0237-0>
- Schmid, S. M., Pfiffner, O.-A., Froitzheim, N., Schönborn, G., & Kissling, E. (1996). Geophysical-geological transect and tectonic evolution of the Swiss-Italian Alps. *Tectonics*, 15(5), 1036–1064. <https://doi.org/10.1029/96tc00433>
- Scholz, C. H. (1998). Earthquakes and friction laws. *Nature*, 391(6662), 37–42. <https://doi.org/10.1038/34097>
- Schwartz, S. Y., & Rokosky, J. M. (2007). Slow slip events and seismic tremor at circum-Pacific subduction zones. *Reviews of Geophysics*, 45(3), RG3004. <https://doi.org/10.1029/2006rg000208>
- Sibson, R. H., Moore, J. M. M., & Rankin, A. (1975). Seismic pumping—A hydrothermal fluid transport mechanism. *Journal of the Geological Society*, 131(6), 653–659. <https://doi.org/10.1144/gsjgs.131.6.0653>
- Siddons, D. P., Kirkham, R., Ryan, C. G., De Geronimo, G., Dragone, A., Kuczewski, A. J., et al. (2014). Maia X-ray microprobe detector array system. *Journal of Physics: Conference Series*, 499, 012001. <https://doi.org/10.1088/1742-6596/499/1/012001>
- Sinclair, H. (1997). Tectonostratigraphic model for underfilled peripheral foreland basins: An Alpine perspective. *Geological Society of America Bulletin*, 109(3), 324–346.
- Tobin, H. J., & Saffer, D. M. (2009). Elevated fluid pressure and extreme mechanical weakness of a plate boundary thrust, Nankai Trough subduction zone. *Geology*, 37(8), 679–682. <https://doi.org/10.1130/g25752a.1>
- Toussaint, R., Aharonov, E., Koehn, D., Gratier, J. P., Ebner, M., Baud, P., et al. (2018). Stylolites: A review. *Journal of Structural Geology*, 114, 163–195. <https://doi.org/10.1016/j.jsg.2018.05.003>
- Ujii, K., & Kimura, G. (2014). Earthquake faulting in subduction zones: Insights from fault rocks in accretionary prisms. *Progress in Earth and Planetary Science*, 1(1), 7. <https://doi.org/10.1186/2197-4284-1-7>
- Ujii, K., Saishu, H., Fagereng, A., Nishiyama, N., Otsubo, M., Masuyama, H., & Kagi, H. (2018). An explanation of episodic tremor and slow slip constrained by crack-seal veins and viscous shear in subduction mélange. *Geophysical Research Letters*, 45(11), 5371–5379. <https://doi.org/10.1029/2018GL078374>
- Vannucchi, P., Remitti, F., Bettelli, G., Boschi, C., & Dallai, L. (2010). Fluid history related to the early Eocene-middle Miocene convergent system of the Northern Apennines (Italy): Constraints from structural and isotopic studies. *Journal of Geophysical Research*, 115(B5), B05405. <https://doi.org/10.1029/2009jb006590>
- Virgo, S., Abe, S., & Urai, J. L. (2014). The evolution of crack seal vein and fracture networks in an evolving stress field: Insights from Discrete Element Models of fracture sealing. *Journal of Geophysical Research: Solid Earth*, 119(12), 8708–8727. <https://doi.org/10.1002/2014JB011520>
- Vrolijk, P. (1990). On the mechanical role of smectite in subduction zones. *Geology*, 18(8), 703–707. [https://doi.org/10.1130/0091-7613\(1990\)018<0703:otmros>2.3.co;2](https://doi.org/10.1130/0091-7613(1990)018<0703:otmros>2.3.co;2)
- Wallace, L. M. (2020). Slow slip events in New Zealand. *Annual Review of Earth and Planetary Sciences*, 48(1), 175–203. <https://doi.org/10.1146/annurev-earth-071719-055104>
- Wallace, L. M., & Beavan, J. (2010). Diverse slow slip behavior at the Hikurangi subduction margin, New Zealand. *Journal of Geophysical Research*, 115(B12), B12402. <https://doi.org/10.1029/2010jb007717>
- Wallace, L. M., Beavan, J., Bannister, S., & Williams, C. (2012). Simultaneous long-term and short-term slow slip events at the Hikurangi subduction margin, New Zealand: Implications for processes that control slow slip event occurrence, duration, and migration. *Journal of Geophysical Research*, 117(B11), B11402. <https://doi.org/10.1029/2012jb009489>
- Wang, K., & Hu, Y. (2006). Accretionary prisms in subduction earthquake cycles: The theory of dynamic Coulomb wedge. *Journal of Geophysical Research*, 111(B6), B06410. <https://doi.org/10.1029/2005JB004094>
- Wichert, J. (2020). Properties of slate. In *Slate as dimension stone* (pp. 61–134). Springer.
- Williams, C. A., Eberhart-Phillips, D., Bannister, S., Barker, D. H. N., Henrys, S., Reyners, M., & Sutherland, R. (2013). Revised interface geometry for the Hikurangi subduction zone, New Zealand. *Seismological Research Letters*, 84(6), 1066–1073. <https://doi.org/10.1785/0220130035>
- Williams, R. T., & Fagereng, A. (2022). The role of quartz cementation in the seismic cycle: A critical review. *Reviews of Geophysics*, 60(1), e2021RG000768. <https://doi.org/10.1029/2021rg000768>